ANL-ART-132

Development of ASME Division 5 Code proposal on temperature limits for simplified design methods

---

Applied Materials Division

About Argonne National Laboratory
Argonne is a U.S. Department of Energy laboratory managed by UChicago Argonne, LLC under contract DE-AC02-06CH11357. The Laboratory's main facility is outside Chicago, at 9700 South Cass Avenue, Argonne, Illinois 60439. For information about Argonne and its pioneering science and technology programs, see www.anl.gov.

DOCUMENT AVAILABILITY

Online Access: U.S. Department of Energy (DOE) reports produced after 1991 and a growing number of pre-1991 documents are available free at OSTI.GOV (http://www.osti.gov/), a service of the U.S. Dept. of Energy's Office of Scientific and Technical Information

Reports not in digital format may be purchased by the public from the National Technical Information Service (NTIS):

U.S. Department of Commerce
National Technical Information Service
5301 Shawnee Rd
Alexandria, VA 22312
www.ntis.gov
Phone: (800) 553-NTIS (6847) or (703) 605-6000
Fax: (703) 605-6900
Email: **orders@ntis.gov**

Reports not in digital format are available to DOE and DOE contractors from the Office of Scientific and Technical Information (OSTI)

U.S. Department of Energy
Office of Scientific and Technical Information
P.O. Box 62
Oak Ridge, TN 37831-0062
www.osti.gov
Phone: (865) 576-8401
Fax: (865) 576-5728
Email: **reports@osti.gov**

Disclaimer
This report was prepared as an account of work sponsored by an agency of the United States Government. Neither the United States Government nor any agency thereof, nor UChicago Argonne, LLC, nor any of their employees or officers, makes any warranty, express or implied, or assumes any legal liability or responsibility for the accuracy, completeness, or usefulness of any information, apparatus, product, or process disclosed, or represents that its use would not infringe privately owned rights. Reference herein to any specific commercial product, process, or service by trade name, trademark, manufacturer, or otherwise, does not necessarily constitute or imply its endorsement, recommendation, or favoring by the United States Government or any agency thereof. The views and opinions of document authors expressed herein do not necessarily state or reflect those of the United States Government or any agency thereof, Argonne National Laboratory, or UChicago Argonne, LLC.

ANL-ART-132

Development of ASME Division 5 Code proposal on temperature limits for simplified design methods

---

Applied Materials Division
Argonne National Laboratory

July 2018

Prepared by

M. C. Messner, Argonne National Laboratory
T.-L. Sham, Argonne National Laboratory

Abstract

This report establishes proposed upper temperature limits for the ASME BP&V Code Section III, Division 5, Nonmandatory Appendix HBB-T design by elastic analysis provisions for bounding ratcheting strain and creep-fatigue damage in Class A high temperature nuclear reactor components. Limitations on the use of these design options are required because the design by elastic analysis methods rely on bounding theories that assume a non-unified, decoupled model of creep-plasticity. However, at high temperatures creep and plastic deformation become coupled and bounding theorems relying a decoupled material response may fail. The report describes a method for selecting appropriate upper temperature limits, demonstrates directly through a comparison to full inelastic simulations that the existing Code provisions can be nonconservative at high temperatures, and develops the requisite Code language required to implement the temperature limits in Section III, Division 5.

Table of Contents

Abstract i
Table of Contents iii
List of Figures v
List of Tables vii
1 Introduction 1
2 Method for establishing temperature limits 3
  2.1 Theory 3
  2.2 Application to the Section III, Division 5, Class A materials 6
    2.2.1 304H 10
    2.2.2 316H 10
    2.2.3 Grade 91 12
    2.2.4 2.25Cr-1Mo 14
    2.2.5 Alloy 800H 16
    2.2.6 A617 19
  2.3 Recommended allowable rate sensitivity, representative strain rate, and temperature limits 21
3 The potential for non-conservatism at high temperatures 23
  3.1 Theoretical background 23
    3.1.1 Primary load design 24
    3.1.2 Deformation controlled quantities: Appendix T 25
  3.2 A demonstration of non-conservatism in an Appendix T strain limits design method 26
    3.2.1 Inelastic model 27
    3.2.2 Comparison to Appendix T strain limits criteria 31
4 Modifications to implement limits in the ASME Code 43
  4.1 Supporting information 43
  4.2 Potential Code changes 43
5 Conclusions 47
  5.1 Effects of implementing the temperature limits 47
  5.2 Summary 47
Acknowledgments 49
Bibliography 51
A An alternative method for determining approximate temperature limits on the HBB-T simplified methods 57
Distribution List 59

List of Figures

2.1 Schematic illustrating a Kocks-Mecking diagram for an idealized material with rate independent and rate dependent deformation regimes. 4
2.2 Kocks-Mecking master diagram for 304H. 11
2.3 3D plot of the flow stress model implied by the Kocks-Mecking master curve for 304H. 11
2.4 Cutoff contours as a function of strain rate and temperature for 304H. Each contour represents a different value of allowable rate sensitivity. 12
2.5 Kocks-Mecking master diagram for 316H. 13
2.6 3D plot of the flow stress model implied by the Kocks-Mecking master curve for 316H. 13
2.7 Cutoff contours as a function of strain rate and temperature for 316H. Each contour represents a different value of allowable rate sensitivity. 14
2.8 Kocks-Mecking master diagram for Grade 91. 14
2.9 3D plot of the flow stress model implied by the Kocks-Mecking master curve for Grade 91. 15
2.10 Cutoff contours as a function of strain rate and temperature for Grade 91. Each contour represents a different value of allowable rate sensitivity. 15
2.11 Kocks-Mecking master diagram for 2.25Cr-1Mo. 16
2.12 3D plot of the flow stress model implied by the Kocks-Mecking master curve for 2.25Cr-1Mo. 16
2.13 Cutoff contours as a function of strain rate and temperature for 2.25Cr-1Mo. Each contour represents a different value of allowable rate sensitivity. 17
2.14 Kocks-Mecking master diagram for Alloy 800H. 17
2.15 3D plot of the flow stress model implied by the Kocks-Mecking master curve for Alloy 800H. 18
2.16 Cutoff contours as a function of strain rate and temperature for Alloy 800H. Each contour represents a different value of allowable rate sensitivity. 18
2.17 Kocks-Mecking master diagram for Alloy 617. 19
2.18 3D plot of the flow stress model implied by the Kocks-Mecking master curve for Alloy 617. 19
2.19 Cutoff contours as a function of strain rate and temperature for Alloy 617. Each contour represents a different value of allowable rate sensitivity. 20

3.1 The response of the reference model under uniaxial tension at a strain rate of $\dot{\varepsilon} = 8.33 \times 10^{-5}\,\mathrm{s}^{-1}$ for several different temperatures. 30
3.2 Example of the creep behavior of the model at $T = 600\,^{\circ}\mathrm{C}$ for several different stresses. 31
3.3 Model behavior in pure fatigue loading at $T = 500\,^{\circ}\mathrm{C}$. The fully-reversed strain range in this example is $\Delta\varepsilon = 0.015$ at a strain rate of $\dot{\varepsilon} = 10^{-3}\,\mathrm{s}^{-1}$. . 38
3.4 Design values of the yield stress (S_y) established for the reference model by simulating a series of uniaxial tension tests. 39

3.5 Design isochronous stress-strain curves constructed for the reference inelastic model. This example is for $T = 550\,^{\circ}\mathrm{C}$. The curves summarize a large number of simulated creep tests. In order from top to bottom the curves are: the hot tensile curve, the isochronous curve for 1 hour, 10 hours, 100 hours, 1,000 hours, 10,000 hours, and 100,000 hours. 39
3.6 Log-linear Larson-Miller correlation between rupture stress, rupture time, and temperature used to set design values of S_r for the reference material model. This correlation was developed by simulating a large number of creep tests at different conditions. 40
3.7 Design fatigue curves for the reference inelastic model at several different temperatures and a strain rate of $\dot{\varepsilon} = 10^{-3}\,\mathrm{s}^{-1}$. Curves are a best-fit polynomial through a series of simulated fatigue tests at different strain ranges. 40
3.8 Design D-diagram for the reference material model. The diagram was constructed by plotting the results of a large series of creep-fatigue experiments, also shown on the figure. 41
3.9 Kocks-Mecking diagram constructed by simulating uniaxial tension and creep tests with the reference inelastic model. 41
3.10 Diagram plotting the ratio between the Appendix HBB-T design life and the time to 1% strain computed by the inelastic model as a function of high cycle temperature. 42

4.1 Comparison between the data underlying the ASME Code values of yield stress (S_y) for the Grade 91 and the Kocks-Mecking model predictions for flow stress at the ASTM E-21 strain rate of $8.33 \times 10^{-5}\,\mathrm{s}^{-1}$. 44

List of Tables

2.1 Summary of experimental database used to establish temperature limits. . . 6
2.2 Summary of data sources compiled to create the Kocks-Mecking diagrams for each material. 7
2.3 Physical constants used to construct Kocks-Mecking diagrams for each of the six materials. 8
2.4 Calibrated coefficients for the Kocks-Mecking models, including root mean square deviation between the experimental data and the model fit. 9
2.5 Table of potential temperature cutoffs for 304H. Cutoff values are in °C. . . 10
2.6 Table of potential temperature cutoffs for 316H. Cutoff values are in °C. . . 13
2.7 Table of potential temperature cutoffs for Grade 91. Cutoff values are in °C. 15
2.8 Table of potential temperature cutoffs for 2.25Cr-1Mo. Cutoff values are in °C. 17
2.9 Table of potential temperature cutoffs for Alloy 800H. Cutoff values are in °C. 18
2.10 Table of potential temperature cutoffs for Alloy 617. Cutoff values are in °C. 20
2.11 Recommended temperature cutoffs for the Division 5 Class A materials and Alloy 617, based on a strain rate of 10^{-7} 1/s and a 10% reduction in flow stress due to rate sensitivity. 21

3.1 Temperature independent parameters for the reference material model. . . . 29
3.2 Temperature dependent parameters for the reference material model. 30
3.3 Temperature limits generated for the reference model using the procedure developed in Chapter 2. Cutoff values are in °C. 34
3.4 Loading conditions, elastic design lives, and inelastic design lives from the consistent comparison between the inelastic model and the corresponding design by elastic analysis. 36

4.1 Recommended Code temperature cutoff table. 44

A.1 Transition temperatures for the Class A materials. 57

1 Introduction

Section III, Division 5 of the ASME Boiler and Pressure Vessel Code establishes rules for the design and construction of high temperature nuclear reactors [6]. The current Code provides two options for evaluating structures against the deformation controlled design limits – excessive cyclic deformation (ratcheting) and creep-fatigue failure: design by inelastic analysis and optional, simplified rules for design by elastic analysis based on structural bounding theories. In practice, at least at the time the Code was developed, the elastic rules were the first choice for evaluating a design, as they are easier and quicker to execute than the design by inelastic analysis methods. If a component could not pass the elastic analysis rules, or if Code provisions excluded applying design by elastic analysis for a particular components, the designer could resort to the inelastic analysis provisions, which are thought to be less overconservative. The design rules for the deformation controlled quantities are in Section III, Division 5, Nonmandatory Appendix HBB-T.

The current Code rules cover five Class A metallic materials: 304H, 316H, 2.25Cr-1Mo, Grade 91, and Alloy 800H. A pending Code Case extends these rules to cover the nickel-based Alloy 617. Currently, the Appendix T design by elastic analysis option can be used for any of these materials at any temperature in the allowable use range.

The design by elastic analysis rules are based on structural bounding theories discussed in detail in Chapter 3 of this report. Several of these bounding theories rely on a non-unified, decoupled theory of creep-plasticity that seperate the total strain rate into elastic, rate-independent plastic, and creep terms:

$$\dot{\boldsymbol{\varepsilon}} = \dot{\boldsymbol{\varepsilon}}_e + \dot{\boldsymbol{\varepsilon}}_p + \dot{\boldsymbol{\varepsilon}}_{cr}. \tag{1.1}$$

Furthermore, decoupled theories assume that there is no link between the elastic, plastic, and creep strain rates except through the current stress state $\boldsymbol{\sigma}$. These types of models assume that prior plasticity does not affect subsequent creep and vice-versa, except by changing the stress.

In actuality, at high temperatures creep and plasticity are coupled deformation mechanisms. In this regime a coupled, unified viscoplastic model better describes the material response. These types of models divide the total strain rate into elastic and viscoplastic contributions

$$\dot{\boldsymbol{\varepsilon}} = \dot{\boldsymbol{\varepsilon}}_e + \dot{\boldsymbol{\varepsilon}}_{vp} \tag{1.2}$$

where the unified viscoplastic term accounts for both creep and plastic deformation.

The assumption of a non-unified model is critical for several of the bounding theories underlying the Appendix T design by elastic analysis rules. As such, viscoplastic material behavior undermines the technical basis for these rules. To prevent potential design nonconservatism limits should be established for the Appendix T design by elastic analysis provisions disallowing their use in the viscoplastic regime.

Comparing equations 1.1 and 1.2 the critical term is the separation of a rate independent plastic strain rate from the rate dependent viscoplastic strain rate. If both creep and plastic deformation become rate sensitive then they would be difficult or impossible to distinguish experimentally. In fact, as described in Chapter 2, in this regime they occur through the same microstructural mechanism. Therefore, the divide between a regime where a decoupled model is physically plausible and where a unified model is required is the point at which plastic deformation becomes rate sensitive.

This report develops a method for finding this threshold. Chapter 2 describes the approach, which uses a physically-based model for the material flow stress and experimental data to find the threshold. The model predicts that the divide between the two regimes is a function of both strain rate and temperature. Therefore, establishing Code upper temperature limits requires selecting a representative strain rate describing a typical plant transient.

With both the flow stress model and a representative strain rate Chapter 2 proposes upper temperature limit on the use of the Appendix T design by elastic analysis provisions for each of the Class A materials plus Alloy 617. Chapter 3 demonstrates that the Appendix T provisions can return nonconservative design lives above the proposed temperature cutoffs using a consistent comparison to a full inelastic analysis. Chapter 4 describes the changes to Section III, Division 5 required to implement the proposed temperature limits. Finally, Chapter 5 discusses the practical effects of adopting temperature limits on the process of Section III, Division 5 design.

2 Method for establishing temperature limits

As argued in the introduction, the upper temperature limit for the bounding design methods in Section III, Division 5 of the ASME Code should be the temperature at which plastic deformation becomes rate dependent. Creep deformation is, by definition, always rate-dependent and so if both plasticity and creep depend on strain rate it will be impossible to discern the two mechanisms.

A method for establishing temperature limits must consider elevated temperatures where both creep and plasticity are operative deformation modes. Furthermore, the relevant strain rate is that of a slow transient, as opposed to the very small strain rates typical of a hold at operating conditions. The cutoffs must consider a transient rate because the component deformation must, at least potentially, involve both plasticity and creep. The ASME Code considers only creep deformation during the course of a hold.

Given these axioms this chapter describes a physically-motivated method for determining the temperature dividing separable creep and rate independent plastic deformation from unified viscoplastic flow. The proposed method references experimental data collated from the literature and DOE reports to determine temperature limits for the five Division 5, Class A Materials as well as Alloy 617.

2.1 Theory

Dislocation motion is the dominant microscale mechanism governing inelastic deformation in all the Class A materials within the allowable ASME operating temperature range. Fundamentally, this implies that creep and plastic deformation are always coupled. However, if creep and plasticity occur in the material under very different conditions – i.e. temperatures and strain rates – dislocations will move on the microscale in two different ways. If plastic deformation is separable from creep, i.e. prior plasticity has no effect on subsequent creep, then a non-unified model can be used to represent the material deformation and the bounds used by the ASME design by elastic analysis methods are applicable.

The standard model of dislocation-controlled plasticity is a dislocation segment moving through a field of short range obstacles. These obstacles can be solute atoms, the Peierls stress, or other forest dislocations. Two forces can propel a dislocation past an obstacle: the applied stress field, resolved as shear on the dislocation's slip system, or random thermal fluctuations that scale with absolute temperature. The thermal fluctuations do not all have a constant amplitude. The longer a dislocation sits pinned at an obstacle the more likely it is to encounter a large thermal oscillation to move it past the barrier. At faster deformation rates a dislocation has less time to sit at any particular barrier. Therefore, thermal activation energy scales inversely proportionally with strain rate.

This simple model of plasticity suggests two deformation regimes. If the applied stress is large enough a dislocation will not need to rely on thermal activation energy to overcome obstacles and the flow stress will not depend on rate or temperature. This is the classical regime of rate independent plasticity. If the applied stress is low some amount of thermal activation energy will be required and the flow stress will depend on both temperature and strain rate. This is the regime of classical rate dependent viscoplasticity.

The model is complicated by the fact that for obstacles fields primarily consisting of other forest dislocations the dislocation stress fields, and hence the energy barrier presented

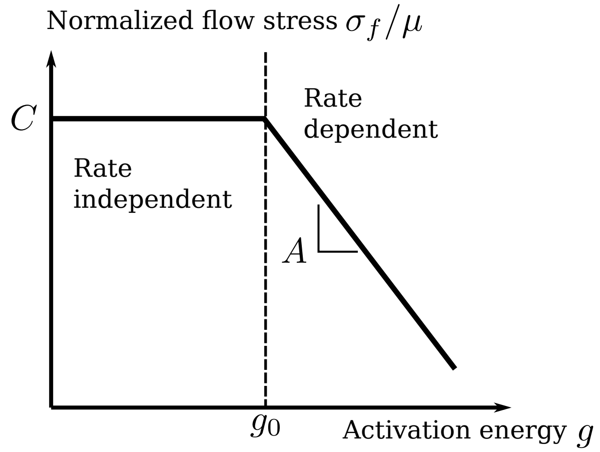

Figure 2.1: Schematic illustrating a Kocks-Mecking diagram for an idealized material with rate independent and rate dependent deformation regimes.

by each obstacle, scales with the temperature dependent material shear modulus. Therefore, the flow stress, normalized by the shear modulus, is temperature independent in the rate independent regime and not the absolute flow stress itself.

If in some component deformation during loading transients occurs in the rate independent regime and deformation during holds occurs in the rate dependent regime then the two deformation mechanisms can be reasonably decoupled. This is the non-unified model assumed by the bounding methods underlying the Division 5 design by elastic analysis approaches. On the other hand, if both transient and steady condition loading occurs in the rate dependent regime then the two cannot be reasonably decoupled. Therefore, upper temperature limits for the Division 5 elastic methods should be based on the transition from the rate-independent to the rate-dependent deformation regimes. This boundary can be expressed equivalently as a value of normalized flow stress or a critical activation energy.

Kocks and Mecking [36, 37, 43] describe the normalized thermal activation energy available for overcoming microstructural obstacles as

$$g = \frac{kT}{\mu b^3} \log \frac{\dot{\varepsilon}_0}{\dot{\varepsilon}}. \tag{2.1}$$

In this expression g is the normalized activation energy, k is the Boltzmann constant, T is absolute temperature, μ is the temperature-dependent shear modulus, b is the Burgers vector, $\dot{\varepsilon}_0$ is a reference strain rate, and $\dot{\varepsilon}$ is the material deformation rate.

Figure 2.1 illustrates a conceptual Kocks-Mecking diagram for a material with rate independent and rate dependent regimes of deformation. The diagram plots the material flow stress, normalized by the shear modulus, as a function of the Kocks-Mecking normalized activation energy. This perfect material has bilinear behavior – a regime with a flat, horizontal response at lower activation energy and a constant negative slope at higher activation energies. The horizontal segment is the rate-independent regime, where the normalized flow stress is independent of activation energy. The portion of the curve with constant, non-zero slope is the rate dependent regime.

In the rate-independent regime the flow stress can be described as

$$\log \frac{\sigma_f}{\mu} = C. \tag{2.2}$$

In the rate-dependent regime the equation of the line is

$$\log \frac{\sigma_f}{\mu} = Ag + B. \tag{2.3}$$

The critical activation energy g_0 separates the two regimes, giving a bilinear model for he material flow stress:

$$\log \frac{\sigma_f}{\mu} = \qquad Cg \leq g_0 \tag{2.4}$$

$$\log \frac{\sigma_f}{\mu} = \qquad Ag + Bg > g_0 \tag{2.5}$$

$$\tag{2.6}$$

Three of the four parameters A, B, C, and g_0 are sufficient to describe the complete model because the two lines must meet at a point. However, we report all four parameters.

Note that the equation describing the rate-dependent flow stress can be recast as

$$\sigma_f = e^B \mu \left(\frac{\dot{\varepsilon}_0}{\dot{\varepsilon}} \right)^{\frac{AkT}{\mu b^3}} \tag{2.7}$$

and therefore the classical rate sensitivity exponent is

$$m = \frac{AkT}{\mu b^3}. \tag{2.8}$$

To establish the temperature limit we are interested in the critical activation energy g_0. Rearranging Eq. 2.1 gives

$$T_0 = \frac{g_0 \mu b^3}{k \log \frac{\dot{\varepsilon_0}}{\dot{\varepsilon}}}. \tag{2.9}$$

Therefore, the transition temperature dividing rate dependent and independent flow depends on the strain rate. Physically, this makes sense in light of the conceptual model for plastic flow described above. The thermal activation energy depends on both temperature and the time a dislocation can remain pinned at an obstacle, which is inversely proportional to strain rate. If the transition is described in terms of temperature only then a representative strain rate must be selected and combined with the Kocks-Mecking parameters in Eq. 2.1. The result of this is a critical temperature T_0 that can be used as the upper temperature limit.

Applying this procedure to real material data requires several steps:

1. Determine the material constants μ (as a function of temperature), b, and $\dot{\varepsilon}_0$.
2. Plot experimental data on a Kocks-Mecking diagram. Determine the g_0 from this data. For actual data this will involve a best-fit optimization.
3. Determine a representative transient strain rate $\dot{\varepsilon}_{ref}$.
4. Use Eq. 2.1 to calculate the temperature cutoff T_0.

The next subsection applies this process to the Class A materials and Alloy 617.

Material	Number of experiments	Number of data points
304H	52	208
316H	290	487
Grade 91	292	953
2.25Cr-1Mo	122	341
Alloy 800H	357	412
Alloy 617	96	97

Table 2.1: Summary of experimental database used to establish temperature limits.

2.2 Application to the Section III, Division 5, Class A materials

Table 2.1 summarizes the experimental data collected from the literature and various material databases. The database includes test records from three different types of experiments: uniaxial tension, creep, and stress relaxation. Table 2.2 summarizes the sources of data used for each material.

Ultimately, the data from each experiment must be processed into a series of (flow stress, strain rate, temperature) tuples. This data can then be plotted on a Kocks-Mecking diagram using Eq. 2.1. Each different type of test requires a different processing procedure. The goal is to produce Kocks-Mecking points representative of the material in the as-received condition before work hardening or softening substantially affects the flow stress.

Uniaxial tension tests were summarized by a collection of (strain, stress) points and meta-data describing the test temperature and strain rate. The post-processing routine calculated the 0.2% offset yield stress from the experimental flow curve. This value is taken as representative of the initial material flow stress. The experiment controls the material temperature and strain rate and so these can be translated directly into the Kocks-Mecking experimental database. Each uniaxial tension test produces one point on a Kocks-Mecking diagram. The material shear modulus, for normalizing the flow stress, was computed using the temperature dependent Young's modulus and Poisson's ratio data in Section II of the ASME Code [3].

Creep tests were summarized as a strain versus time history along with meta-data describing the stress applied to the specimen and the temperature. The creep rate versus time history was determined by finite differencing from the creep versus time data. The initial rate of primary creep was used as representative of the material in the as-received condition. The initial creep rate is largely unaffected by material work hardening or softening, particularly for low applied loads near or below the yield stress. The test temperature and the flow stress are controlled. Again, the ASME elastic properties were used to compute the temperature dependent shear modulus. Each creep test produces a single point on the Kocks-Mecking diagram.

Stress relaxation data was recorded as a stress versus time relaxation profile with meta-data describing the test temperature. In stress relaxation experiments the total strain is held fixed. This implies the relation

$$0 = \dot{\varepsilon} = \dot{\varepsilon}_e + \dot{\varepsilon}_{in} \tag{2.10}$$

Material	Source	Material	Source
304H	Chen and Argon [19]	2.25Cr-1Mo	Klueh and Oakes [35]
	Chavez et al. [18]		Klueh [34]
	Krempl [39]		Swindeman and Klueh [54]
	Yamashita and Wada [63]		Swindeman and Klueh [55]
316H	Albertini et al. [2]	Grade 91	Asayama and Tachibana [7]
	DeSisto and Carr [21]		Choudhary and Isaac Samuel [20]
	Fookes et al. [23]		Kim and Weertman [32]
	Hammond and Sikka [26]		Kimura et al. [33]
	Horak et al. [27]		Koo and Kwon [38]
	Hormozi et al. [28]		Latha et al. [40]
	Kanazawa and Yoshida [30]		Maruyama et al. [42]
	Kim et al. [31]		Swindeman [52]
	Mizuno [45]		Swindeman [53]
	Mohanty et al. [46]		Yaguchi and Takahashi [61]
	Ohno et al. [49]		Yaguchi and Takahashi [62]
	Sikka et al. [51]		Zhang and Aktaa [66]
	Takahashi et al. [56]	Alloy 800H	Idaho National Laboratory
	Wang et al. [58]		Oak Ridge National Laboratory
	Wood and Williamson [59]		Ohba et al. [48]
	Wood et al. [60]	Alloy 617	Agarwal et al. [1]
	Yoon et al. [64]		Idaho National Laboratory
	Youtsos et al. [65]		Osthoff et al. [50]
	Zhu et al. [67]		

Table 2.2: Summary of data sources compiled to create the Kocks-Mecking diagrams for each material.

Material	b	$\dot{\varepsilon}_0$
304H	$2.019 \times 10^{-7}\,\mathrm{mm}$	$10^{5}\,\mathrm{s}^{-1}$
316H	$2.019 \times 10^{-7}\,\mathrm{mm}$	$10^{5}\,\mathrm{s}^{-1}$
Grade 91	$2.474 \times 10^{-7}\,\mathrm{mm}$	$10^{10}\,\mathrm{s}^{-1}$
2.25Cr-1Mo	$2.474 \times 10^{-7}\,\mathrm{mm}$	$10^{10}\,\mathrm{s}^{-1}$
Alloy 800H	$2.474 \times 10^{-7}\,\mathrm{mm}$	$10^{10}\,\mathrm{s}^{-1}$
Alloy 617	$2.474 \times 10^{-7}\,\mathrm{mm}$	$10^{5}\,\mathrm{s}^{-1}$

Table 2.3: Physical constants used to construct Kocks-Mecking diagrams for each of the six materials.

with $\dot{\varepsilon}_e$ the elastic strain rate and $\dot{\varepsilon}_{in}$ the inelastic strain rate. For uniaxial loading

$$\dot{\varepsilon}_e = \frac{\dot{\sigma}}{E} \tag{2.11}$$

with E the material Young's modulus. Combining Eqs. 2.10 and 2.11 gives an expression for the inelastic strain rate

$$\dot{\varepsilon}_{in} = -\frac{\dot{\sigma}}{E} \tag{2.12}$$

as a function of the stress rate and the material Young's modulus. The stress rate was calculated for each experiment by finite differencing the stress versus time relaxation profile. The material temperature dependent Young's modulus was taken from Section II of the ASME Code [3]. Each point on the relaxation curve then corresponds to a (flow stress, inelastic strain rate, temperature) point. Each such point can be related to a single point on the Kocks-Mecking diagram. A stress relaxation experiment then actually corresponds to a line on the Kocks-Mecking diagram. This line was sampled discretely with 10 individual, equally spaced points. Therefore, in the current procedure a stress relaxation test produces 10 points on the Kocks-Mecking diagram.

Table 2.3 lists the Burgers vector used in the Kocks-Mecking relation for each of the six materials. These Burgers vectors were computed using the alloy's crystal system (face centered cubic or body centered cubic for these materials) and the lattice coefficient. The shear modulus was computed from the ASME temperature dependent elastic properties.

The values of the bilinear model (A, B, C, and g_0) along with the reference strain rate were computed using a two-stage optimization procedure. For a given value of reference strain rate, $\dot{\varepsilon}_0$ the experimental data for a particular material can be converted into a series of points on a Kocks-Mecking diagram. A nonlinear least squares optimization procedure can be used to find the best fit parameters for the bilinear model. The root mean square deviation (RMSD) between the model and the experimental data can be computed. A meta-parameter optimization procedure was used to final the value of reference strain rate that minimizes the RMSD between the data and the bilinear Kocks-Mecking model for each of the six materials. This simple meta-parameter optimization procedure computed the RMSD for 12 decades of reference strain rate spanning from $10^{0}\,\mathrm{s}^{-1}$ to $10^{11}\,\mathrm{s}^{-1}$ to find the value that minimized the RMSD. Table 2.3 lists the optimal values of the reference strain rate for each material.

Material	A	B	g_0	C	RMSD
304H	-2.252	-4.546	0.6880	-6.095	0.190
316H	-1.844	-4.456	0.6936	-5.735	0.301
Grade 91	-8.064	-2.177	0.3522	-5.023	0.158
2.25Cr-1Mo	-7.920	-2.251	0.4331	-5.681	0.149
Alloy 800H	-6.600	-2.376	0.5743	-6.167	0.295
Alloy 617	-9.092	-2.167	0.3573	-5.410	0.321

Table 2.4: Calibrated coefficients for the Kocks-Mecking models, including root mean square deviation between the experimental data and the model fit.

The results of this procedure are the parameters describing the best-fit bilinear Kocks-Mecking model for each of the materials. Table 2.4 summarizes these results. The table also shows the minimum value of RMSD between the experimental data and the best-fit bilinear model. The bilinear model can be plotted over the experimental points on a Kocks-Mecking diagram. For example, Fig. 2.2 shows this plot for 304H stainless steel.

To provide additional information, used in selecting appropriate values for the representative transient strain rate and the final temperature limits, the procedure described in Section 2.1 was modified slightly. The bilinear Kocks-Mecking model for the flow stress as a function of activation energy can be plotted in temperature/strain rate space by expanding the equation for the Kocks-Mecking normalized activation energy. Figure 2.3 shows an example of this type of plot for 304H. Plotted in this form the rate-independent region appears as a plateau of constant normalized flow stress. The rate dependent region is a drop-off in flow stress from the rate-independent plateau. The lip of the plateau is the dividing line between rate-independent and rate-dependent flow. This dividing curve is a function of temperature and strain rate.

The Section III, Division 5 design by elastic analysis procedures will not immediately become non-conservative when plastic deformation becomes rate sensitive. Though the procedures rely on bounding methods assuming a non-unified model of creep-plasticity they also make a large number of conservative assumptions about the material properties. A procedure for generating temperature limits for these methods could use these conservative assumptions to justify allowing some amount of material rate sensitivity before setting the temperature limit. One method to do this is by allowing rate sensitivity to reduce the flow stress somewhat from the rate-independent plateau.

We considered three different values of allowable rate sensitivity, expressed as percentage reductions from the rate-independent normalized flow stress: 0% (i.e. no allowable rate sensitivity), 10%, and 20%. These values can be visualized as contours on the flow stress relation in rate-temperature space, shown in red on Fig. 2.3.

Each contour, projected onto the rate-temperature plane, is a potential Code boundary separating rate sensitive from rate insensitive deformation. As an example, Fig. 2.4 shows these potential boundaries for 304H. For a selected representative strain rate each contour provides a different value of the temperature cutoff.

In the process of making a decision as to which values of allowable rate sensitivity and representative strain rate to select we generated potential temperature cutoffs for five values

	100%	90%	80%
$10^{-4}\,\mathrm{s}^{-1}$	740	779	815
$8.33 \times 10^{-5}\,\mathrm{s}^{-1}$	735	774	811
$10^{-5}\,\mathrm{s}^{-1}$	683	722	759
$10^{-6}\,\mathrm{s}^{-1}$	631	672	708
$10^{-7}\,\mathrm{s}^{-1}$	582	625	662

Table 2.5: Table of potential temperature cutoffs for 304H. Cutoff values are in °C.

of strain rate: $10^{-4}\,\mathrm{s}^{-1}$, $10^{-5}\,\mathrm{s}^{-1}$, $8.33 \times 10^{-5}\,\mathrm{s}^{-1}$, $10^{-6}\,\mathrm{s}^{-1}$, and $10^{-7}\,\mathrm{s}^{-1}$. These values span expected transient strain rate for common high temperature reactor concept designs. The particular value of $8.33 \times 10^{-5}\,\mathrm{s}^{-1}$ is the strain rate prescribed by the ASTM E-21 procedure for high temperature uniaxial tension testing [8]. The data underlying the ASME values of yield stress, S_y, were mostly collected following this procedure.

The result of this process is a matrix of potential temperature cutoffs spanning the three values of allowable rate sensitivity and the five values of potential representative strain rates. Table 2.5 lists these values for 304H. These data were used to determine which values of allowable rate-sensitivity and representative strain rates to select in recommending the final temperature cutoffs.

The subsequent subsections reference, briefly describe, and comment on the Kocks-Mecking information and the matrix of potential cutoffs for the six materials under consideration.

2.2.1 304H

Figure 2.2 is the Kocks-Mecking diagram for 304H. Figure 2.3 is the 3D flow stress plot and Fig. 2.4 are the contours describing potential temperature limits. Table 2.5 is the matrix of potential temperature cutoffs.

304H has a relatively high error between the experimental data and the model. There are several factors contributing to the high error: relatively high batch variation in the underlying experimental database, work hardening in 304H allowing experimentalists to conduct accelerated creep tests at stresses well above the yield stress, and a relatively limited amount of available experimental data compared to some of the other materials. Batch and product form variations directly increase the scatter in the underlying data. Creep tests conducted above the yield stress are not representative of the material in the as-received condition. Potentially these data should be excluded from the Kocks-Mecking diagram, however because of the limited amount of available data they were retained when calibrating the flow stress model. Despite this relatively high error we have confidence in the temperature cutoffs based on corroborating information described in Chapter 4.

2.2.2 316H

Figure 2.5 is the Kocks-Mecking diagram for 316H. Figure 2.6 is the 3D flow stress plot and Fig. 2.7 are the contours describing potential temperature limits. Table 2.6 is the matrix of potential temperature cutoffs.

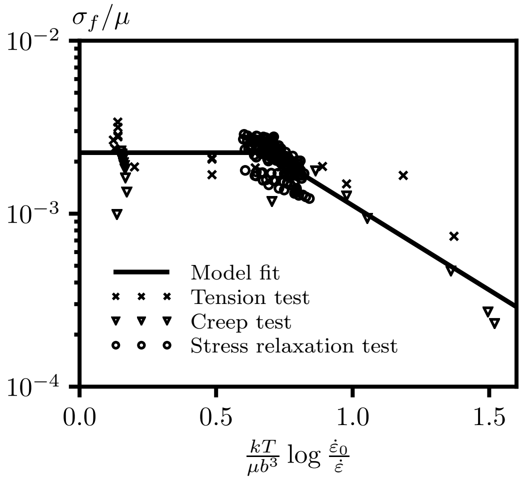

Figure 2.2: Kocks-Mecking master diagram for 304H.

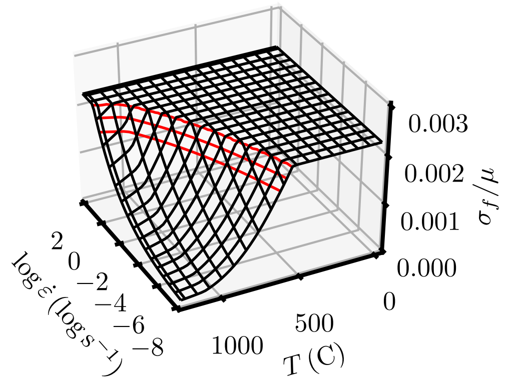

Figure 2.3: 3D plot of the flow stress model implied by the Kocks-Mecking master curve for 304H.

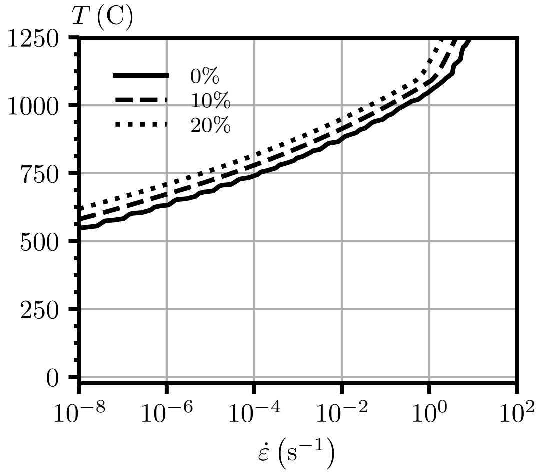

Figure 2.4: Cutoff contours as a function of strain rate and temperature for 304H. Each contour represents a different value of allowable rate sensitivity.

There is a large amount of scatter in the data collected for 316H. However, we were also able to identify a large quantity of data and so we have high confidence in the final temperature cutoffs. Previous work [51] shows extremely large batch-to-batch and product form variation in measured values of yield stress and ultimate tensile stress for 316H. One reason for this is significant chemical variations from heat to heat. It is not surprising then that the flow stress model also shows considerable scatter. The Section III approach is nominally applicable to all allowable product forms and so our approach of finding the best-fit average material rate sensitivity is reasonable for determining temperature limits for the design by elastic analysis procedures. Additional scatter in the Kocks-Mecking plot is introduced by creep tests conducted well above the material yield stress, as described in the subsection summarizing the 304H results.

The Kocks-Mecking diagram for 316H (Fig. 2.5) clearly shows a third, linear regime of behavior at low activation energies. The data in this regime was collected at very high strain rates using Hopkinson bar tests [65]. There is a good physical explanation for a third, rate dependent regime at high strain rate. For very high rate loading the dislocation mobility can govern the material flow stress. Free dislocation motion is opposed by lattice friction, often represented as linear viscous drag. For FCC materials this lattice friction is very low and so for most engineering strain rates dislocations move essentially instantaneously between obstacles, at least relative to the amount of time required for a dislocation to bypass an obstacle once pinned. However, at fast strain rates ($\gtrapprox 10^1\,\mathrm{s}^{-1}$) this lattice friction can itself set the material flow stress, by requiring a high stress to move dislocations through the lattice quickly enough to maintain the fast, imposed deformation rate. Hopkinson bar tests sample this deformation regime.

2.2.3 Grade 91

Figure 2.8 is the Kocks-Mecking diagram for Grade 91. Figure 2.9 is the 3D flow stress plot and Fig. 2.10 are the contours describing potential temperature limits. Table 2.7 is the

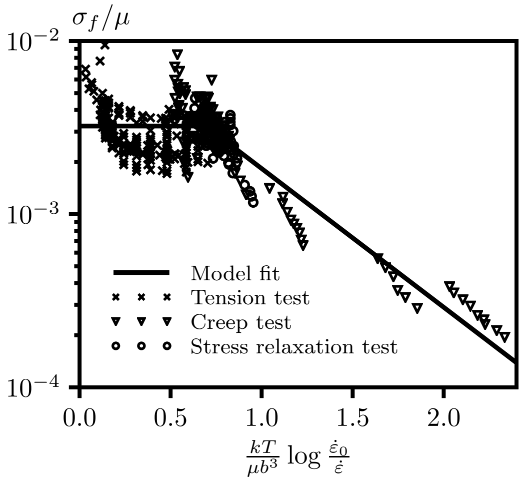

Figure 2.5: Kocks-Mecking master diagram for 316H.

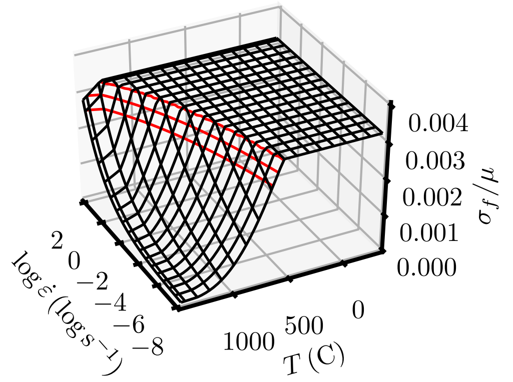

Figure 2.6: 3D plot of the flow stress model implied by the Kocks-Mecking master curve for 316H.

	100%	90%	80%
$10^{-4}\,\mathrm{s}^{-1}$	739	790	834
$8.33 \times 10^{-5}\,\mathrm{s}^{-1}$	734	785	829
$10^{-5}\,\mathrm{s}^{-1}$	692	734	777
$10^{-6}\,\mathrm{s}^{-1}$	632	683	727
$10^{-7}\,\mathrm{s}^{-1}$	586	637	681

Table 2.6: Table of potential temperature cutoffs for 316H. Cutoff values are in °C.

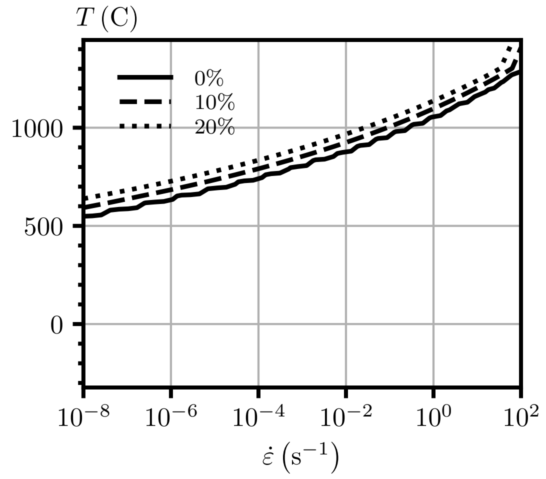

Figure 2.7: Cutoff contours as a function of strain rate and temperature for 316H. Each contour represents a different value of allowable rate sensitivity.

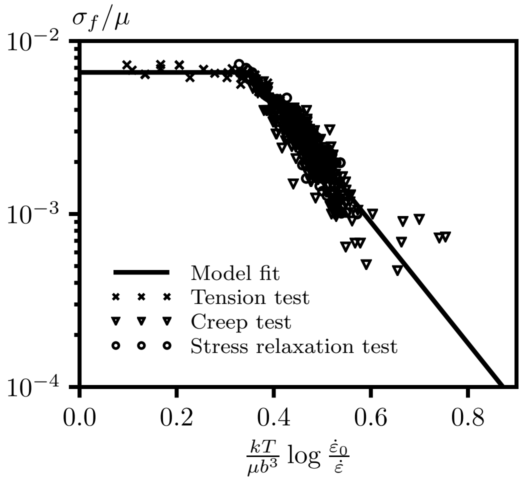

Figure 2.8: Kocks-Mecking master diagram for Grade 91.

matrix of potential temperature cutoffs.

Grade 91 has relatively low error between the Kocks-Mecking model and the experimental results. This material is work softening at moderately elevated temperatures, meaning all the creep tests were conducted at or below the yield stress.

2.2.4 2.25Cr-1Mo

Figure 2.11 is the Kocks-Mecking diagram for 2.25Cr-1Mo. Figure 2.12 is the 3D flow stress plot and Fig. 2.13 are the contours describing potential temperature limits. Table 2.8 is the matrix of potential temperature cutoffs.

The error between the flow stress model and the data is relatively small. As with Grade 91 this material is work softening at relatively low temperatures so creep tests were conducted at or below the yield stress and the resulting data is representative of the material in the

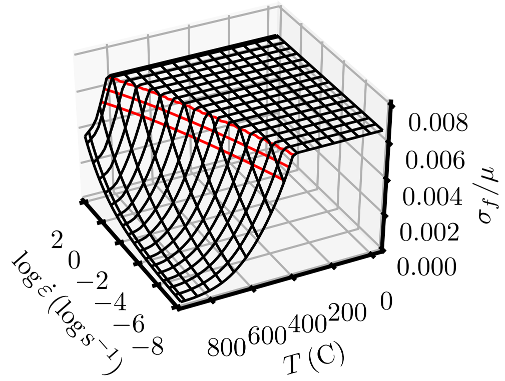

Figure 2.9: 3D plot of the flow stress model implied by the Kocks-Mecking master curve for Grade 91.

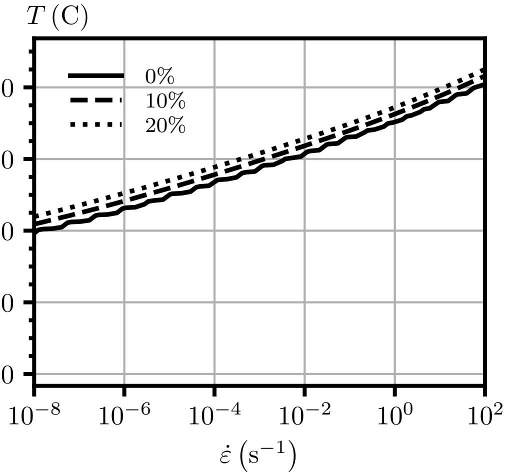

Figure 2.10: Cutoff contours as a function of strain rate and temperature for Grade 91. Each contour represents a different value of allowable rate sensitivity.

	100%	90%	80%
$10^{-4}\,\mathrm{s}^{-1}$	535	556	576
$8.33\times10^{-5}\,\mathrm{s}^{-1}$	528	553	574
$10^{-5}\,\mathrm{s}^{-1}$	499	518	540
$10^{-6}\,\mathrm{s}^{-1}$	462	482	504
$10^{-7}\,\mathrm{s}^{-1}$	425	448	470

Table 2.7: Table of potential temperature cutoffs for Grade 91. Cutoff values are in °C.

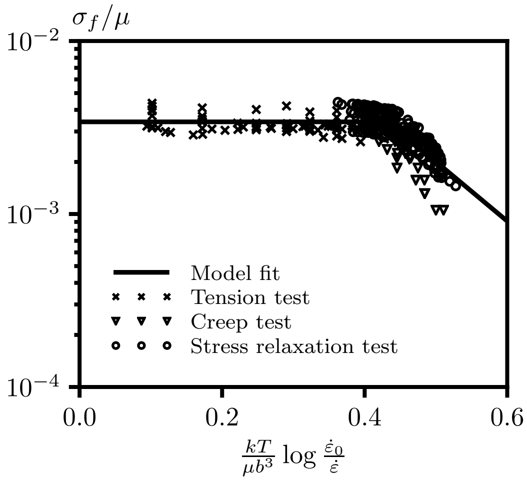

Figure 2.11: Kocks-Mecking master diagram for 2.25Cr-1Mo.

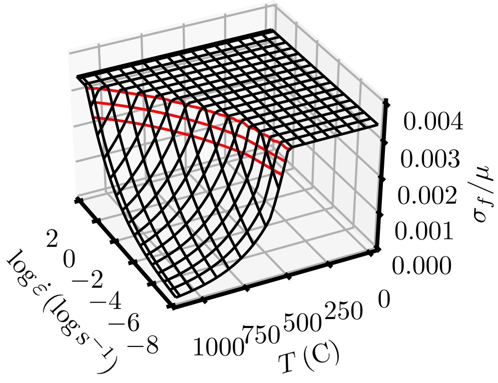

Figure 2.12: 3D plot of the flow stress model implied by the Kocks-Mecking master curve for 2.25Cr-1Mo.

as-received condition.

2.2.5 Alloy 800H

Figure 2.14 is the Kocks-Mecking diagram for Alloy 800H. Figure 2.15 is the 3D flow stress plot and Fig. 2.16 are the contours describing potential temperature limits. Table 2.9 is the matrix of potential temperature cutoffs.

The error between the model and the data is relatively high for this material. 800H is work hardening up to relatively high temperatures and so the creep test data encompasses experiments conducted above the yield stress. Additionally, the material shows relatively large batch-to-batch and product form variations. However, the Kocks-Mecking model clearly captures the transition from rate sensitive to rate insensitive deformation, which is the critical feature for establishing temperature cutoffs.

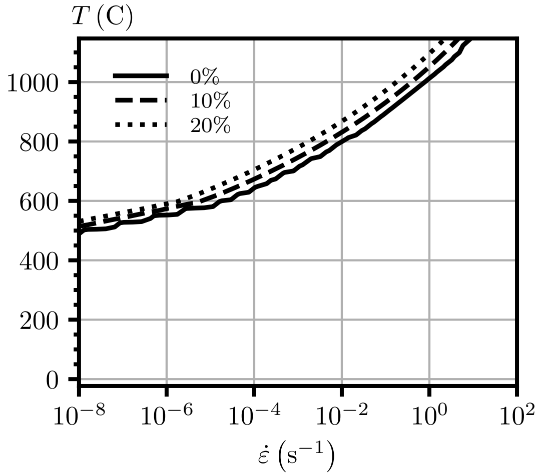

Figure 2.13: Cutoff contours as a function of strain rate and temperature for 2.25Cr-1Mo. Each contour represents a different value of allowable rate sensitivity.

	100%	90%	80%
$10^{-4}\,\mathrm{s}^{-1}$	643	672	704
$8.33 \times 10^{-5}\,\mathrm{s}^{-1}$	633	667	698
$10^{-5}\,\mathrm{s}^{-1}$	579	610	639
$10^{-6}\,\mathrm{s}^{-1}$	552	573	590
$10^{-7}\,\mathrm{s}^{-1}$	527	543	560

Table 2.8: Table of potential temperature cutoffs for 2.25Cr-1Mo. Cutoff values are in °C.

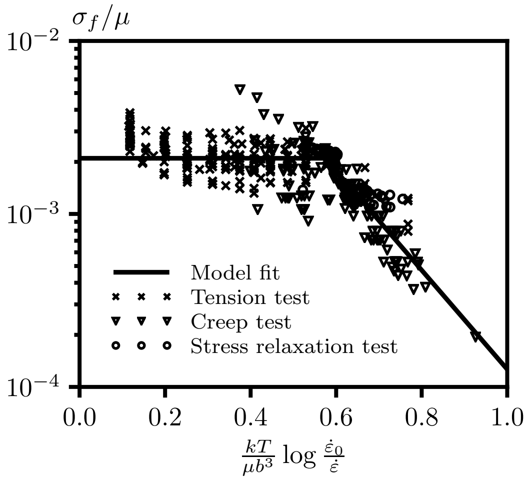

Figure 2.14: Kocks-Mecking master diagram for Alloy 800H.

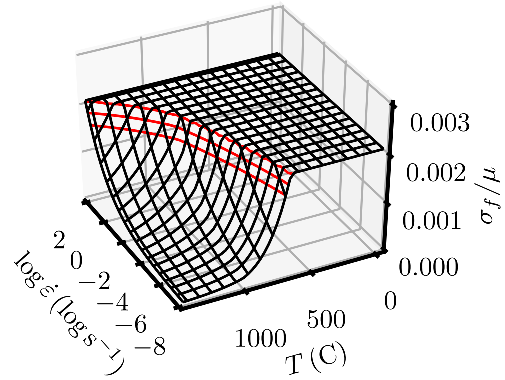

Figure 2.15: 3D plot of the flow stress model implied by the Kocks-Mecking master curve for Alloy 800H.

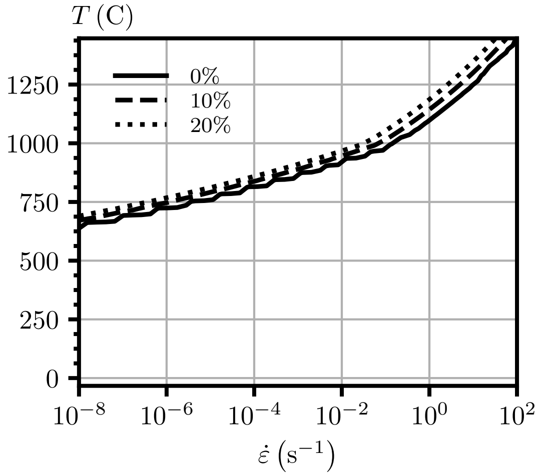

Figure 2.16: Cutoff contours as a function of strain rate and temperature for Alloy 800H. Each contour represents a different value of allowable rate sensitivity.

	100%	90%	80%
10^{-4} s^{-1}	815	837	858
8.33×10^{-5} s^{-1}	814	833	854
10^{-5} s^{-1}	758	790	811
10^{-6} s^{-1}	724	746	767
10^{-7} s^{-1}	691	708	727

Table 2.9: Table of potential temperature cutoffs for Alloy 800H. Cutoff values are in °C.

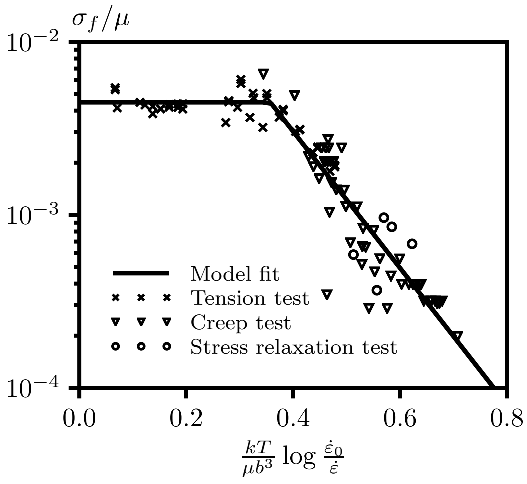

Figure 2.17: Kocks-Mecking master diagram for Alloy 617.

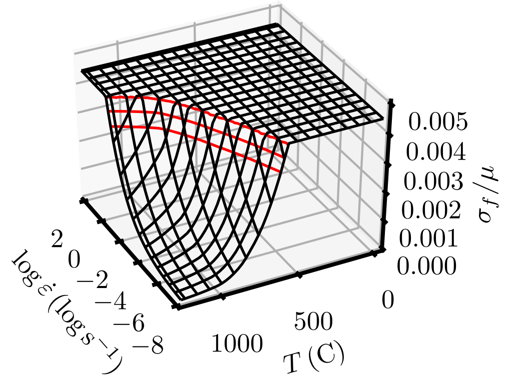

Figure 2.18: 3D plot of the flow stress model implied by the Kocks-Mecking master curve for Alloy 617.

2.2.6 A617

Figure 2.17 is the Kocks-Mecking diagram for Alloy 617. Figure 2.18 is the 3D flow stress plot and Fig. 2.19 are the contours describing potential temperature limits. Table 2.10 is the matrix of potential temperature cutoffs.

Error is relatively high for this material, which likely reflects the relatively limited amount of data identified and collected. However, the diagram clearly captures the transition between rate sensitive and rate insensitive deformation. Additional information, described in Chapter 4 corroborates the final cutoff temperature selected for Alloy 617.

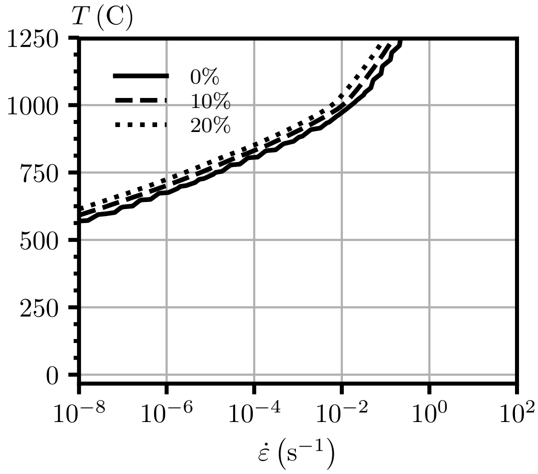

Figure 2.19: Cutoff contours as a function of strain rate and temperature for Alloy 617. Each contour represents a different value of allowable rate sensitivity.

	100%	90%	80%
$10^{-4}\,\mathrm{s}^{-1}$	806	831	851
$8.33 \times 10^{-5}\,\mathrm{s}^{-1}$	805	826	846
$10^{-5}\,\mathrm{s}^{-1}$	737	764	787
$10^{-6}\,\mathrm{s}^{-1}$	675	701	724
$10^{-7}\,\mathrm{s}^{-1}$	621	644	667

Table 2.10: Table of potential temperature cutoffs for Alloy 617. Cutoff values are in °C.

Material	Cutoff (°C)
304H	625
316H	640
Grade 91	450
2.25Cr-1Mo	550
Alloy 800H	710
Alloy 617	645

Table 2.11: Recommended temperature cutoffs for the Division 5 Class A materials and Alloy 617, based on a strain rate of $10^{-7}\,{}^{1}\!/\!_{\mathrm{s}}$ and a 10% reduction in flow stress due to rate sensitivity.

2.3 Recommended allowable rate sensitivity, representative strain rate, and temperature limits

From the available matrix of allowable reductions from the rate-independent flow stress and potential representative transient strain rates we elected to use a 90% reduction and a representative rate of $10^{-7}\,\mathrm{s}^{-1}$. The allowable reduction was selected based on engineering judgement, assessing the effect of the conservative assumptions in the implementation of the Appendix T design design by elastic analysis methods compared to the underlying theoretical bounding methods, and by corroborating information described in Chapter 4. The representative strain rate was selected by surveying typical transients in high temperature reactors. The transient rate was selected to bound slow transients in many different types of high temperature reactors, though the available data mostly focuses on sodium cooled fast reactors. Note that the bounding transient is the slowest representative transient, not the fastest, because slower strain rates allow more time for thermal activation, lowering the temperature required to push the material into the rate sensitive regime. This trend can be clearly seen in the matrix of potential cutoffs developed for each material.

Table 2.11 summarizes the recommended temperature cutoffs for each of the five Section III, Division 5, HBB Class A metallic materials plus Alloy 617. The potential effects of adopting these cutoffs and the required Code changes needed to implement these cutoffs are described in further detail in Chapter 4.

3 The potential for non-conservatism at high temperatures

The introduction to this report stated that the Section III, Division 5 design by elastic analysis methods may be non-conservative in deformation regimes where a decoupled model of creep plasticity cannot represent the material's response. At sufficiently high temperatures non-unified models break down and must be replaced by unified viscoplastic models explicitly linking creep and plastic deformation. However, the introduction did not explicitly demonstrate why the design by elastic analysis methods rely on non-unified creep plasticity. This chapter demonstrates why the Code bounding methods rely on such non-unified models.

The first section of this chapter traces the theoretical background underlying the Section III, Division 5 design by elastic analysis methods back to a set of theoretical bounds on material behavior. Many of these bounds were made starting from a theoretical model of material response that assumes non-unified creep-plasticity. The second section then uses a comparison to full inelastic analysis to demonstrate one particular design provision in Section III, Division 5 may be non-conservative above the proposed temperature cutoffs.

3.1 Theoretical background

Section III, Division 5 of the ASME Code guards against six potential elevated temperature failure mechanisms:

1. Time-independent plastic instability
2. Time-dependent creep rupture
3. Creep-fatigue damage
4. Time-dependent, cyclic excessive deformation (ratcheting)
5. Time-independent buckling
6. Time-dependent buckling.

The Code groups the first two into the "primary load design." For design by elastic analysis the design procedures guarding against the second two mechanisms, creep-fatigue damage and ratcheting, are co-dependent and use similar bounding methods, grouped as "deformation controlled quantities" in the Code. This section examines the underlying bounding methods used in the Code for primary load and the deformation controlled quantities to evaluate their reliance on a decoupled, non-unified theory of creep plasticity. This analysis identifies any potential theoretical non-conservatism in the Code design methods. However, the Code approaches make additional, conservative assumptions beyond the underlying theoretical bounds. These additional conservative assumptions may cause the Code procedures to remain conservative even in regions of behavior where the theoretical bounds are not applicable (e.g. in regions where a non-unified creep-plasticity model does not describe the material response.

3.1.1 Primary load design

The Code primary load design method relies on a theoretical stationary stress distribution developed in the component after a long period of creep and plastic deformation. The Section III, Division 5 procedure calls this steady state of stress the primary load and compares it to allowable stress intensities designed to guard against plastic instability and creep rupture. These allowable stresses include factors designed to bound the worst-case material behavior.

The Code definition of primary load is strictly any state of stress in equilibrium with the applied forces, reaction forces from fixed constraints. This definition is a historical relic. When the Code rules were originally developed computing the actual stationary stress distribution was difficult or impossible for many structural components. Instead, an approach based on Timoshenko-type [57] shell theory was adopted where the primary stress distribution was analyzed by assuming sufficient relaxation of the actual kinematic constraints to make the problem statically determinate. The stresses resulting from this statically determinate problem were called the primary stresses. The total elastic stress field could then be solved by superimposing the stresses resulting from reimposing kinematic constraints on the individual, determinant sections of the structure to bring the parts back into compatibility. Because the choice of where to relax the kinematic constraints is arbitrary primary load analysis is described in the Code as finding any stress field that is in equilibrium with the applied forces. Note that this procedure only produces an approximation to the actual stationary stress distribution and not the actual stationary stresses for any particular material model.

So the underlying theoretical questions are:

1. Is the assumption of some stationary stress state reasonable for all material descriptions, both unified and non-unified models of creep-plasticity?

2. If so, does the Code primary load analysis procedure represent the actual stationary stresses with approximately equal accuracy for non-unified and unified models of creep-plasticity?

The authors are not aware of any detailed theoretical studies examining the effect of different constitutive assumptions on the development or non-development of stationary stresses under some constant, applied loading. However, intuitively any “saturating” material theory will predict the eventual development of a stationary stress state. Saturating here means that a material point under constant applied stress eventually reaches a constant, steady strain rate. This implies that internal variables representing the material’s inelastic response eventually saturate. For physically-based theories this might mean the material microstructure evolves towards some equilibrium configuration

Clearly power law and Norton-Bailey creep models are saturating. Creep models that use internal variables to evolve from some non-constant primary stress state towards a constant secondary creep rate are saturating. Rate independent theories of plasticity are also saturating. Any combination of saturating creep theories and rate independent plasticity will be saturating. This covers most non-unified theories of creep-plasticity.

Not all realistic material models predict a saturating response. For example, a model that incorporates creep damage will not predict the development of a steady state of stress.

However, the majority of unified inelastic constitutive models not designed to represent material degradation mechanisms will predict a saturating material response [16].

The answer to the second question posed above is more difficult and may merit further study. On initial inspection there is no reason to think the Code process for finding the primary stress distribution will be any more or less accurate in the viscoplastic regime than it is in the regime where a non-unified model is appropriate.

Overall then, it is unlikely the Section III, Division 5 procedure for primary load design will be non-conservative at high temperatures where creep and plastic deformation are coupled.

3.1.2 Deformation controlled quantities: Appendix T

Section III, Division 5, Nonmandatory Appendix HBB-T contains rules for evaluating structures against the "deformation controlled" creep-ratcheting and creep-fatigue damage design limits using elastic or inelastic analysis. The Appendix T rules for design by elastic analysis are based on three seminal bounding theories. The first bound was developed by Frederick and Armstrong [24]. In this work Frederick and Armstrong establish that any standard constitutive model will eventually reach a steady state of stress under cyclic loading. In this steady state the stresses and strain rates in the material become periodic. The derivation presented in the main body of the text [24] is for a non-unified model of creep-plasticity, but the authors extend it to any Drucker-stable [22] material in an appendix. Therefore, the Appendix T elastic analysis rules can rely on a structure reaching some cyclic steady state, even in the unified creep-plasticity range.

The Frederick-Armstrong theory does not address what the steady-state cycle response will be for any particular structure. To bound the steady cycle the Code relies on the work of Bree [9, 10]. Bree categorized the steady state response of a structure under cyclic loading into four categories:

1. Elastic: the structure remains elastic at all times. The accumulated strains in the structure remain bounded.
2. Elastic shakedown: after some initial plasticity the steady state cyclic response is entirely elastic. The accumulated strain remains bounded.
3. Plastic shakedown: the steady state cycle involves plastic deformation but the accumulated strain remains bounded.
4. Ratcheting: the strains in the structure increase without bound.

The Code endeavours to place structures into one of categories 1-3. If the structure shakes down the ratcheting strain design criteria can be met by finding a bound on the net accumulated strain at any point in the structure. This bound can be compared to the Code strain accumulation design criteria.

Bree's original derivation used an elastic-perfectly plastic material model and a particular structure – an open-ended tube. Subsequent work extended the model to work hardening rate-independent plasticity and other structural configurations. Bree, and the ASME Code, argues that the original Bree diagram for an open-ended tube bounds the response of actual structures. As such, references to the Bree diagram in the ASME Code refer to Bree's original diagram.

There is good evidence that the original Bree diagram bounds work hardening rate independent plasticity and cylindrical vessels with end caps [9, 10]. To our knowledge there has been no extension of the original Bree diagram to consider various unified creep-plasticity models. Therefore, there is no direct evidence that the Bree diagram used in the Appendix T procedure describes or bounds the steady-state cyclic response of a realistic component with a unified, viscoplastic constitutive response.

The final bounding theorem invoked by the Appendix T elastic analysis rules is that of O'Donnell and Porowski [47]. O'Donnell and Porowski observed that in the Bree steady state shakedown solutions there is a portion of the vessel wall that remains linear elastic through the entire loading history. They used this concept of an elastic core to bound the creep deformation accumulated over a section during some design life by computing the creep strain corresponding to the maximum elastic stress in the core. They argue that this accumulated creep must bound the sectional response.

The O'Donnell-Porowski approach explicitly requires a non-unified creep-plasticity model. The core stress approach assumes that creep and plastic deformation couple only through the stress state, which excludes unified viscoplastic models. Additionally, the idea of an elastic core relies on Bree's original analysis which, as noted above, may not be valid for a unified viscoplastic material response. The core stress concept underlies many of the HBB-T design methods.

This implies that the O'Donnell-Porowski bound may not hold for a viscoplastic material. Additionally, the Appendix T design by elastic analysis creep-fatigue damage bounds use the idea of an elastic core stress to compute strain ranges and further assume a decoupled creep model when calculating stress relaxation profiles. As such, the Appendix T design by elastic analysis creep-fatigue rules may also not be bounding when the structure responds viscoplastically.

3.2 A demonstration of non-conservatism in an Appendix T strain limits design method

The previous section notes there are theoretical flaws in two of the methods used in Appendix T to bound ratcheting strain accumulation and creep-fatigue damage. This section applies one of the design options in Appendix T to a particular problem to directly show that it can be non-conservative at elevated temperatures where the material response is viscoplastic.

The method used to demonstrate this potential non-conservatism is a comparison to a full inelastic analysis. First, we define a reference inelastic model. This reference model behaves reasonably, i.e. its material response is plausible for a structural material in elevated temperature service. The material model is viscoplastic – creep and plastic deformation are coupled and represented with a unified inelastic strain rate. The model captures details of cyclic plasticity through backstress evolution equations. Furthermore, the model includes a damage model that represents material failure under either constant stress (creep) loading, cyclic fatigue loading, or a combination of creep and fatigue. The key idea is that this inelastic model behaves like a real structural material.

Because this model has a complete, realistic response we can use the material model to simulate the experiments used to establish Section III, Division 5 design data. This includes uniaxial tension, creep, fatigue, and creep-fatigue tests. This synthetic experimental data can then be used to construct design curves following the standard ASME methodology. These design curves are consistent with the inelastic model – they represent the model's deformation and failure characteristics.

With this consistent design data we can compare a full inelastic analysis of a structure to the corresponding Section III, Division 5 design calculations. This comparison is fair and consistent – the design data used in the calculations exactly represents the full inelastic model. If the ASME design methods fail to return a conservative design life, compared to the inelastic calculation, we can reasonably attribute this failure to some fundamental flaw in the design methods. Put another way, if the Code design procedures cannot safely bound the simulated response of a structure where there are no uncertainties in material response, component dimensions, loading conditions, etc. then the Code provisions will likely also have difficulty bounding the response of a real component at similar loading conditions.

Furthermore, this approach has several advantages over a direct comparison to component test or in-service failure data. One advantage was already noted – there are no uncertainties. For example, the same finite element model could be used in the full inelastic simulation and the compute the elastic stresses used in the Section III design calculations. The design data perfectly corresponds to the reference inelastic material response and so no safety factors need to be applied to the design data to bound material uncertainties, batch-to-batch variation, or different product processing conditions.

The inelastic model need not represent one of the existing HBB Class A metallic materials. It must only produce a reasonable material response for an elevated temperature structural material. That is, the reference inelastic model must plausibly represent some material that designers may want included in the ASME Code – not an existing Code material.

This approach of verifying design methods by consistent inelastic analysis is a powerful tool that could be applied to most of the design rules in the ASME Code or other elevated temperature design methods. The verification check produced by this method is a necessary but not sufficient bound. The consistent comparison tests the underlying bounding theorems with perfect information on the material response, structural geometry, and loading conditions available. Actual design codes must also consider material and structural uncertainty as well as consideration of an appropriate design margin. Therefore, this method cannot entirely replace experimental and component testing. But it does serve as a fast screening tool to identify potential flaws with design methods.

3.2.1 Inelastic model

The reference inelastic model used here builds on a formulation for describing material rate sensitivity across a wide range of structural conditions developed in previous work [44]. This model uses Kocks-Mecking diagrams, like those developed in Chapter 2, to determine if, for a particular set of loading conditions, a model should apply a rate-independent or rate-dependent response.

The model uses a unified viscoplastic framework, decomposing the strain rate as

$$\dot{\boldsymbol{\varepsilon}} = \dot{\boldsymbol{\varepsilon}}_e + \dot{\boldsymbol{\varepsilon}}_{vp}. \tag{3.1}$$

The elastic strains are linearly related to the stress rate through an elasticity tensor **C**

$$\dot{\boldsymbol{\varepsilon}}_e = \mathbf{C}^{-1} \cdot \dot{\boldsymbol{\sigma}}. \tag{3.2}$$

The inelastic strain switches between a rate independent and a rate dependent response depending on the loading conditions. This switch is based on the Kocks-Mecking normalized activation energy

$$g = \frac{kT}{\mu b^3} \log \frac{\dot{\varepsilon}_0}{\dot{\varepsilon}} \tag{3.3}$$

$$\dot{\boldsymbol{\varepsilon}}_{vp} = \begin{cases} \dot{\boldsymbol{\varepsilon}}_{ri} & g \leq g_0 \\ \dot{\boldsymbol{\varepsilon}}_{rd} & g > g_0 \end{cases} \tag{3.4}$$

where g_0 is the same constant used in the rate sensitivity criteria developed in Chapter 2. The rate independent update is defined as

$$\dot{\boldsymbol{\varepsilon}}_{ri} = \gamma \frac{\partial f}{\partial \boldsymbol{\sigma}} \tag{3.5}$$

$$\gamma \geq 0 \tag{3.6}$$

$$f\left(\boldsymbol{\sigma}, \boldsymbol{h}, \sigma_0\right) \leq 0 \tag{3.7}$$

$$\gamma f\left(\boldsymbol{\sigma}, \boldsymbol{h}, \sigma_0\right) = 0 \tag{3.8}$$

$$\gamma \dot{f}\left(\boldsymbol{\sigma}, \boldsymbol{h}, \sigma_0\right) = 0 \tag{3.9}$$

and the rate dependent update is defined by

$$\dot{\boldsymbol{\varepsilon}}_{rd} = \gamma \frac{\partial f}{\partial \boldsymbol{\sigma}} \tag{3.10}$$

$$\gamma = \left\langle \frac{f^n}{\eta} \right\rangle. \tag{3.11}$$

In these expressions f is some function used as a yield surface for the rate independent update and a flow function for the rate dependent update and **h** is some generic set of internal variables. For the rate independent update the initial yield stress is

$$\sigma_0 = \mu e^C \tag{3.12}$$

where the constants are defined in Chapter 2. For the rate dependent update the parameters are

$$\sigma_0 = 0 \tag{3.13}$$

$$n = -\frac{\mu b^3}{kTA} \tag{3.14}$$

$$\eta = e^B \mu \dot{\varepsilon}_0^{kTA/\left(\mu b^3\right)} \tag{3.15}$$

again where the parameters are defined in the previous chapter.

Parameter	Value
A	-1.844
B	-7.014
C	-5.735
g_0	0.6936
$\dot{\varepsilon}_0$	$10^5\,\mathrm{s}^{-1}$
b	$2.019 \times 10^{-7}\,\mathrm{mm}$

Table 3.1: Temperature independent parameters for the reference material model.

This particular model uses a standard J_2 flow rule with isotropic hardening variable σ_i and kinematic hardening backstress $\boldsymbol{X}$

$$f = J_2\left(\boldsymbol{\sigma} - \boldsymbol{X}\right) - \sqrt{\frac{2}{3}}\sigma_i. \tag{3.16}$$

The isotropic hardening model is temperature dependent Voce

$$\dot{\sigma_i} = Q\delta e^{-\delta\bar{\varepsilon}_{vp}}\dot{\bar{\varepsilon}}_{vp} \tag{3.17}$$

where Q and δ are temperature dependent parameters and $\bar{\varepsilon}_{vp}$ is the equivalent inelastic strain. The kinematic hardening uses Chaboche's model [17]

$$\mathbf{X} = \sum_{i=1}^{n} \mathbf{X}_i \tag{3.18}$$

$$\dot{\mathbf{X}}_i = \left(\frac{2}{3}C_i\mathbf{n} - \sqrt{\frac{2}{3}}\gamma_i\left(\bar{\varepsilon}_{vp}\right)\mathbf{X}_i\right)\dot{\gamma} \tag{3.19}$$

in this case with two backstresses ($n = 2$). Here C_i and γ_i are temperature-dependent parameters.

The reference inelastic model combines this model for viscoplastic flow with a model designed to represent creep and fatigue damage. This model modifies the stress update defined previously

$$\hat{\sigma} = (1 - \omega)\sigma. \tag{3.20}$$

The specific damage model used here is a combination of the classical Leckie-Hayhurst-Kachanov [29, 41] model for creep damage and a modified power law model used to represent fatigue damage:

$$\dot{\omega} = \left(\frac{\hat{\sigma}_e}{K_1}\right)^{\chi}\frac{1}{\left(1-\omega\right)^{\phi}} + \frac{\left(\omega + K_2\right)^{a}\sigma_e}{W_0}\dot{\bar{\varepsilon}}_{vp}. \tag{3.21}$$

Here $\hat{\sigma}_e$ is the effective stress $\sigma_e = \sqrt{3J_2\left(\boldsymbol{\sigma}\right)}$ and K_1, χ, ϕ, K_2, W_0, and a are all temperature dependent material parameters.

Table 3.1 lists the temperature independent material properties used for the reference material model. The temperature dependent elastic and thermal expansion coefficients are those for 316H stainless steel in Section II of the ASME Code. Table 3.2 lists the remaining

Parameter	25° C	300° C	500° C	600° C	800° C
Q	700 MPa	400 MPa	350 MPa	300 MPa	300 MPa
δ	2.4	2.4	2.4	2.4	2.4
C_1	1450 MPa	1500 MPa	1900 MPa	1900 MPa	1900 MPa
γ_1	14	14	80	80	80
C_2	1250 MPa	1250 MPa	1250 MPa	1250 MPa	1250 MPa
γ_2	6	6	20	20	20
K_1	11700 MPa	5070 MPa	2470 MPa	1560 MPa	715 MPa
χ	26.4	13.7	10.2	9.00	7.32
ϕ	24.0	24.0	24.0	24.0	24.0
K_2	10^{-3}	10^{-3}	10^{-3}	10^{-3}	10^{-3}
W_0	800 MPa	600 MPa	300 MPa	150 MPa	150 MPa
a	1.25	1.25	1.25	1.25	1.25

Table 3.2: Temperature dependent parameters for the reference material model.

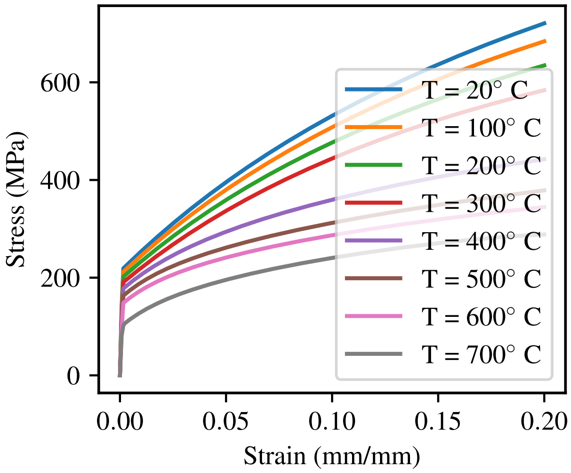

Figure 3.1: The response of the reference model under uniaxial tension at a strain rate of $\dot{\varepsilon} = 8.33 \times 10^{-5}\,\mathrm{s}^{-1}$ for several different temperatures.

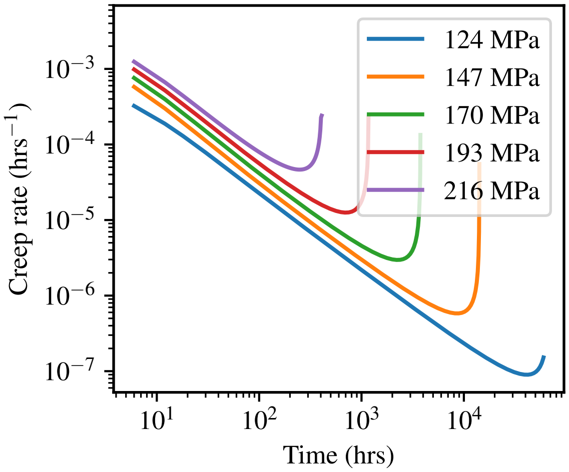

Figure 3.2: Example of the creep behavior of the model at $T = 600\,^{\circ}\mathrm{C}$ for several different stresses.

temperature dependent parameters. The model linearly interpolates parameters for temperatures in between those in the table.

Figure 3.1 plots the model response to uniaxial tension at a fixed strain rate for a variety of temperatures. The model is work hardening, like the austenitic stainless steels 304H and 316H. The temperature-dependent flow curves show reasonable trends of a decreasing initial yield stress and decreased work hardening as temperature increases.

The creep damage model causes the model to fail under sustained constant stress. Figure 3.2 shows several creep curves, plotted as creep rate versus time, for different stresses at 600° C. Increasing the stress generally increases the creep rate and decrease the time to rupture.

Finally, Fig. 3.3 shows two representations of the results of simulating pure fatigue loading. Subfigure (a) plots the maximum and minimum cycles stresses versus cycle count. The reference material model is cyclic hardening. The modified power law damage model accelerates damage accumulation near the end of life so that the reference inelastic model, realistically, rather abruptly fails after a prolonged period of approximately steady maximum and minimum cycle stress. A simple power law damage model would instead decrease the peak stresses more or less uniformly through the course of the simulation Subfigure (b) plots the same data as stress/strain hysteresis loops.

3.2.2 Comparison to Appendix T strain limits criteria

3.2.2.1 Developing design data for the reference model

Conducting a consistent comparison between this reference inelastic model and the HBB design procedures requires developing consistent design data. The HBB-T approach requires the following temperature dependent design data:

1. Yield stress S_y
2. Time-independent allowable stress S_m, which requires the ultimate tensile stress S_{uts}.

3. Time and temperature dependent rupture stress S_r
4. Time dependent allowable stresses S_t and S_{mt}
5. Isochronous stress-strain curves
6. Fatigue curves
7. A creep-fatigue interaction diagram.

Additionally, to test the hypothesis that the Appendix T methods are non-conservative at high temperatures we need to establish a cutoff temperature for the reference material model following the procedure developed in Chapter 2.

The temperature dependent yield stress, ultimate tensile stress, and allowable S_m can be established by simulating a series of uniaxial tension tests at different temperatures and at the fixed, ASTM E-21 strain rate of $8.33 \times 10^{-5}\,\mathrm{s}^{-1}$. Figure 3.4 plots the yield stress S_y determined from this series of simulations. The ultimate tensile stress is only required for determining the time independent allowable S_m. Following the procedures in Section II of the ASME Code for this material

$$S_m = \min\left\{\frac{9}{10}S_y, \frac{2}{3}S_{uts}\right\}. \tag{3.22}$$

Note that the Code uses a bounding procedure based on the specified room temperature minimum yield stress when developing S_y as a function of temperature. Because there is no material variation in the inelastic model this bounding procedure is not necessary for the reference material data.

Isochronous stress strain curves are a way to interpret the results of a large series of creep tests. These curves plot stress versus strain at fixed time through a sequence of creep tests conducted at the same temperature but different levels of stress. For the reference model these curves can be easily constructed by simulating a large series of creep tests and rearranging the resulting strain versus time data. Figure 3.5 shows an example of one of the resulting isochronous stress-strain curves at 550 °C. Similar curves were constructed throughout the creep temperature range for the fictitious material at 25 °C increments. The Code uses the average material response when constructing isochronous curves.

Conventionally, the ASME Code constructs creep-rupture lives from experimental data by constructing a Larson-Miller correlation to the data. For actual experimental data this correlation is designed as a lower bound. However, here we can use the raw simulated data directly because the damage model was calibrated to yield a log-linear rupture life correlation on a Larson-Miller plot. Figure 3.6 shows the simulated creep-rupture data and the resulting Larson-Miller correlation. The agreement between the Larson-Miller model and the synthetic data is nearly perfect. The small discrepancy is because the Hayhurst damage model used in the reference inelastic model obeys a Larson-Miller relation if the parameter χ scales as the inverse of the absolute temperature. In between temperature control points the model interpolates this parameter linearly, which does not exactly agree with the $1/T$ Larson-Miller scaling. The log-linear Larson-Miller correlation shown on the plot is used to generate values for the rupture stress S_r.

Fatigue curves in Section III, Division 5 are plotted as cycles to failure versus strain range. Figure 3.7 shows fatigue curves constructed for the reference inelastic model by simulating a series of strain-controlled fatigue experiments to failure at several different temperatures and strain ranges. The strain rate used in the simulations, $10^{-3}\,\mathrm{s}^{-1}$ is typical of the data used to construct the fatigue curves for the actual Class A materials. The lines on the diagram is a polynomial log-log fit to the simulated data. These lines are used as the design data when executing the consistent comparison to the Code design rules. The agreement between this interpolated curves and the underlying synthetic data is good. The actual Code fatigue curves apply a factor of 2 to the experimental strain ranges and 20 to the experimental cycles to failure data. These factors are designed to account for material uncertainty, product form and batch-to-batch variation, and environmental effects. None of these are relevant for the consistent comparison to the reference inelastic model and so these factors are omitted in the fatigue curves.

Section III, Division 5 considers creep-fatigue damage interaction using a damage or D-diagram. These diagrams plot fatigue damage, computed with Miner's rule as

$$D_f = \sum \frac{N}{N_f} \tag{3.23}$$

where N is the number of loading cycles and N_f is the number of cycles to failure at the cycle strain range, computed using the design fatigue curves, with the sum over the number of cycle types, versus creep damage computed with a time fraction rule

$$D_c = \int \frac{1}{t_r} dt \tag{3.24}$$

where t_r is the time to rupture at given stress and the integral covers the entire load-history.

The design D-diagram is an envelope – the designer plots the computed creep damage and the computed fatigue damage. If the point is inside the envelope the design passes the creep-fatigue check. If the point falls outside the envelope the design fails.

A database of creep-fatigue tests at different strain ranges, hold times, and temperatures is used to develop a D-diagram for a new material. Given a rupture stress relation and a set of fatigue curves the creep and fatigue damages for each creep-fatigue test are computed and plotted. For actual materials the average material response, not the Code lower bounds, are used to compute the creep and fatigue damage when making the D-diagram. Here this is not a concern as the rupture and fatigue diagrams already represent average material behavior. A damage envelope is drawn on the plot following the average material response. As logically this envelope must pass through the (1,0) and (0,1) points on the D-diagram the envelope is often expressed as an intersection point of two straight lines on the damage diagram. Figure 3.8 shows the design D-diagram and the underlying set of simulated creep-fatigue tests for the reference inelastic material model. The design intersection point was selected as (0.1,0.1) based on this data.

Finally, to evaluate the efficacy of the procedure for determining upper temperature cutoffs developed in the previous chapter we must also develop a temperature cutoff for the reference inelastic material model. The procedure can be followed exactly as developed in Chapter 2 using simulated uniaxial tension and simulated creep tests. Figure 3.9 shows

	100%	90%	80%
$10^{-4}\,\mathrm{s}^{-1}$	601	642	684
$8.33 \times 10^{-5}\,\mathrm{s}^{-1}$	597	637	680
$10^{-5}\,\mathrm{s}^{-1}$	544	584	628
$10^{-6}\,\mathrm{s}^{-1}$	492	531	575
$10^{-7}\,\mathrm{s}^{-1}$	446	483	527

Table 3.3: Temperature limits generated for the reference model using the procedure developed in Chapter 2. Cutoff values are in °C.

the Kocks-Mecking plot developed for the ficticious material. Table 3.3 shows the resulting matrix of potential cutoff temperatures. As described previously, we recommend using a 90% reduction from the rate-independent normalized flow stress and a representative strain rate of $10^{-7}\,\mathrm{s}^{-1}$. Using these values, the temperature cutoff for the reference inelastic material model is $T_0 = 483\,^\circ\mathrm{C}$.

3.2.2.2 Evaluating HBB-T-1322 Test B-1

Appendix HBB-T has a wide variety of options for evaluating designs against the ratcheting strain and creep-fatigue design criteria. To assess the effect of a unified, viscoplastic material response of the appendix we started by performing a consistent comparison to evaluate HBB-T-1322 Test B-1. This is an option for checking a design against the ratcheting strain criteria. This test is a good starting point for evaluating the HBB design by elastic analysis methods because it is the direct implementation of the well-documented O'Donnell-Porowski [47] procedure for bounding ratcheting strain accumulation. The bounding method was described in detail in a previous section.

The Code implementation of the approach considers a single loading cycle where the average wall temperature of a vessel cycles between T_L and T_U under a constant primary load. There are Code rules for combining loading cycles but these are not considered here. The basic steps in the Code procedure are:

1. Classify the stresses and determine the primary stress intensity P and secondary stress intensity Q.

2. Compute the non-dimensional Bree coordinates $X = \frac{P}{S_{yL}}$ and $Y = \frac{Q}{S_{yL}}$ where S_{yL} is the value of S_y corresponding the low cycle average wall temperature.

3. Consult the O'Donnell-Porowski diagram to find the factor Z corresponding to the Bree coordinate (X,Y).

4. Find the elastic core stress $\sigma_c = f Z \sigma_{yL}$ where $f = 1.25$ in the Code procedure.

5. To find the accumulated ratcheting strain consult the material isochronous stress-strain curves at stress σ_c and the material design life t_{life}. The accumulated inelastic strain is the strain corresponding to this time and stress.

6. If this strain is less than 1% (for base material) the structure passes the Code check and is deemed to pass the ratcheting strain design check. This strain is supposed to represent the average section accumulated inelastic ratcheting strain.

The factor of $f = 1.25$ in this procedure is designed to move the core stress from one computed with the Code values of S_y, which represent a lower bound material property, to the average material property. Because the inelastic model and corresponding design curves all represent the average material properties when we carry out the consistent comparison we neglect this factor, i.e. $f = 1.0$ and use the actual material yield stress σ_y in the calculations.

The corresponding full inelastic calculation is to simulate the response of the component under the load history using the full inelastic material model. At the end of the design history compute the average section inelastic strain. If this quantity exceeds 1% then the design would fail the Code ratcheting strain criteria. The inelastic design life can be found by sequentially applying more and more cycles until the simulation predicts an accumulation of greater than 1% strain.

Because all the design factors have been removed from the design data and the design analysis procedure a good result would be if the Code design-by-elastic analysis design life exactly matches the design life calculated with the full inelastic model. For actual structures the design factors in the elastic analysis procedures would bound material and loading uncertainties and provide a margin to account for unknown or unexpected failures.

There is an additional requirement for the O'Donnell-Porowski approach that the loading cycle must be anchored in the negligible creep regime. The Code enforces this requirement by requiring that the low cycle wall temperature T_L be less than the temperature at which the Code time dependent allowable S_t for 100,000 hours design life equals the Code time independent allowable stress S_m. For the reference inelastic material model this temperature is $535\,^{\circ}\mathrm{C}$.

The component geometry used to assess the Code design procedure is a Bree cylinder – an open-ended, thin-walled, cylindrical pressure vessel. This geometry is easy to simulate for the full inelastic model and simplifies the stress classification procedure. The particular load cycle used here is a linear, through wall thermal gradient. On the cold side of the cycle the temperature is constant through the vessel wall at $T = T_L$. At the hot side of the cycle there is a linear gradient from $T = T_U$ on the inside of the vessel to $T = T_L$ on the outside. In addition, the vessel is subject to a constant pressure p.

For this simple geometry and loading the primary stress intensity is $P = \frac{pr}{t}$ where r is the vessel radius and t is the vessel wall thickness. The secondary stress intensity is $Q = \int_{T_L}^{T_H} \alpha E dT$ where α is the material's temperature-dependent thermal expansion coefficient and E is the material's temperature-dependent Young's modulus.

The load cycle selected for this comparison starts at several different values of T_L both above and below the proposed cutoff temperature T_0. For each load case the upper temperature is $T_U = T_L + 25\,^{\circ}\mathrm{C}$.

This information, plus the design database described in the previous subsection, is sufficient to execute HBB-T-1322 Test B-1. For each initial temperature T_L the primary load intensity was varied so that the design life returned by the HBB-T-1322 procedure was approximately 60,000 hours. Table 3.4 shows the load cycles used for the consistent comparisons.

T_L (°C)	T_U (° C)	X	Y	$t_{elastic}$ (hrs)	$t_{inelastic}$ (hrs)
400	425	0.528	1.80	60892	192421
425	450	0.487	1.83	62110	96892
450	475	0.448	1.86	63834	52344
475	500	0.409	1.90	64900	36344
500	525	0.374	1.93	62878	22636
525	550	0.340	1.97	62152	18645
575	600	0.283	2.03	63891	14056

Table 3.4: Loading conditions, elastic design lives, and inelastic design lives from the consistent comparison between the inelastic model and the corresponding design by elastic analysis.

To execute a corresponding full inelastic simulation two additional pieces of information are required. The abstract load cycle must be divided into a series of load-hold-unload steps. Assuming a linear temperature ramp and using the same ramp rate for both the temperature increase and decrease two additional parameters fully-define the loading sequence: the temperature ramp rate $\dot{T}$ and the hold time t_{hold}. The example calculation summarized here uses $\dot{T} = 10\,^{\circ}\mathrm{C/hr}$ and $t_{hold} = 1200\,\mathrm{hrs}$. However, we considered several different values for these parameters and they do not affect the final conclusions.

Table 3.4 shows the design life comparisons between the reference inelastic simulations and the consistent Appendix T design calculation.

Figure 3.10 plots the data as a ratio between the inelastic design life, $t_{inelastic}$ and the elastic design life, $t_{elastic}$. If this ratio is greater than one the elastic analysis method is conservative, that is it predicts a shorter design life than the actual reference simulation. If the ratio is less than one the elastic analysis is not conservative – it predicts a longer design life than the reference simulation. The results show that the design by elastic analysis method transitions from being conservative at temperatures below the suggested upper temperature limits to being nonconservative above the proposed cutoff. This is direct evidence that at least one of the bounding design by elastic analysis methods becomes nonconservative above the proposed upper temperature limits.

The limitation imposed on the test – that the low temperature side of the cycle be anchored in the negligible creep regime – does not prevent the problem. This temperature is labeled on the diagram. There is a significant range of non-conservative results in between the proposed upper temperature limit and this preexisting temperature limitation.

While this example only examines one of many options provided by Appendix HBB-T similar bounding methods underlie the other design by elastic analysis methods. This example clearly demonstrates the potential need for imposing some upper temperature limits on the HBB-T design methods.

This example stripped the design factors applied at several points in the design by elastic analysis procedures. Some of these factors are clearly designed to bound material uncertainty, which is not an issue in the consistent comparison. These factors tend to be very conservative and likely mean that the design provisions remain conservative even above the proposed cutoffs, at least in the case of an average material response. However, relying on factors designed to guard against material uncertainty to prevent nonconservatism caused by a more fundamental flaw in the design procedures undermines the intent of the factors and risks an unsafe design for structures with a below average material response.

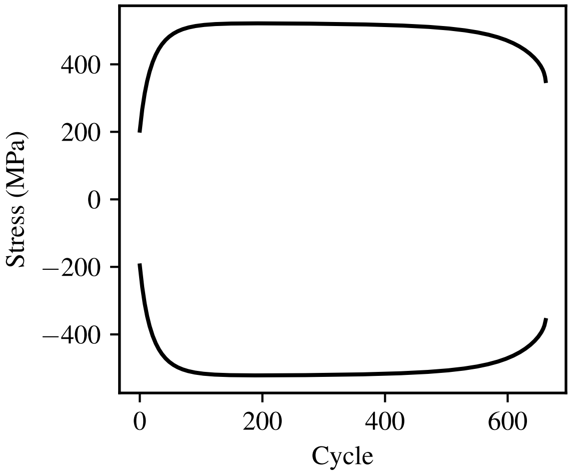

(a) Maximum and minimum stress versus cycle count.

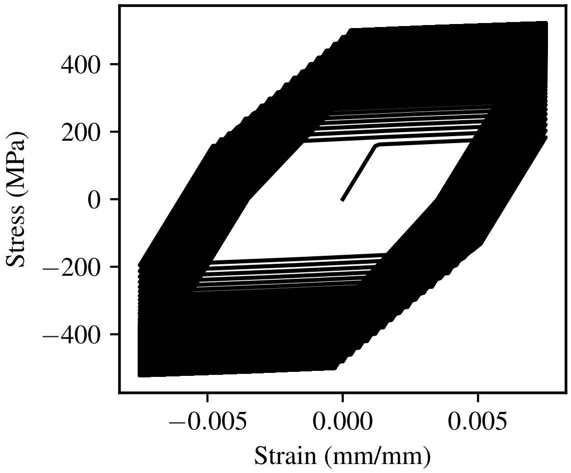

(b) Stress/strain hysteresis loops.

Figure 3.3: Model behavior in pure fatigue loading at $T = 500\,^{\circ}\mathrm{C}$. The fully-reversed strain range in this example is $\Delta\varepsilon = 0.015$ at a strain rate of $\dot{\varepsilon} = 10^{-3}\,\mathrm{s}^{-1}$.

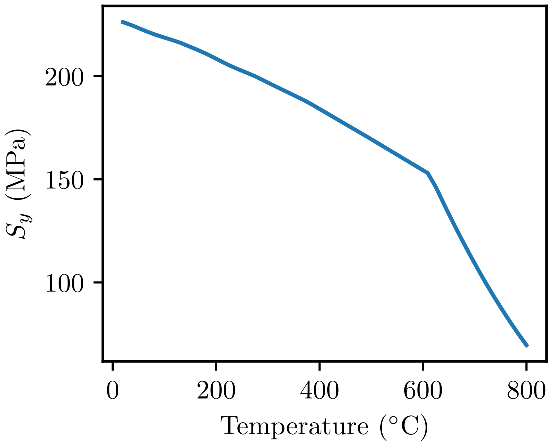

Figure 3.4: Design values of the yield stress (S_y) established for the reference model by simulating a series of uniaxial tension tests.

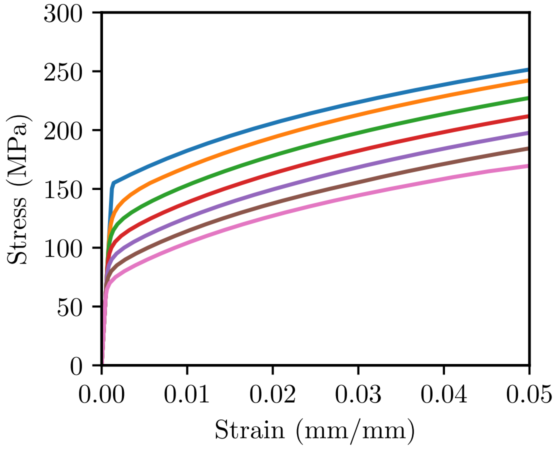

Figure 3.5: Design isochronous stress-strain curves constructed for the reference inelastic model. This example is for $T = 550\,^\circ\mathrm{C}$. The curves summarize a large number of simulated creep tests. In order from top to bottom the curves are: the hot tensile curve, the isochronous curve for 1 hour, 10 hours, 100 hours, 1,000 hours, 10,000 hours, and 100,000 hours.

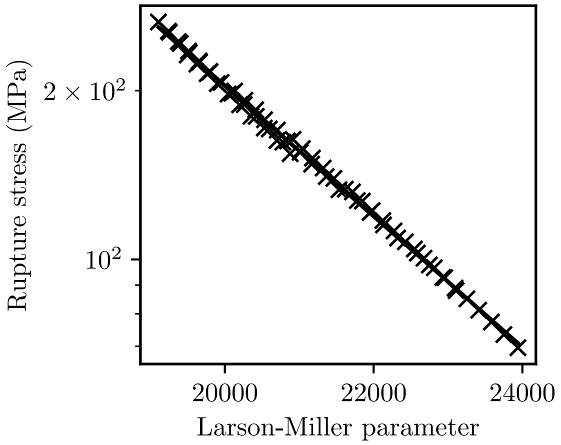

Figure 3.6: Log-linear Larson-Miller correlation between rupture stress, rupture time, and temperature used to set design values of S_r for the reference material model. This correlation was developed by simulating a large number of creep tests at different conditions.

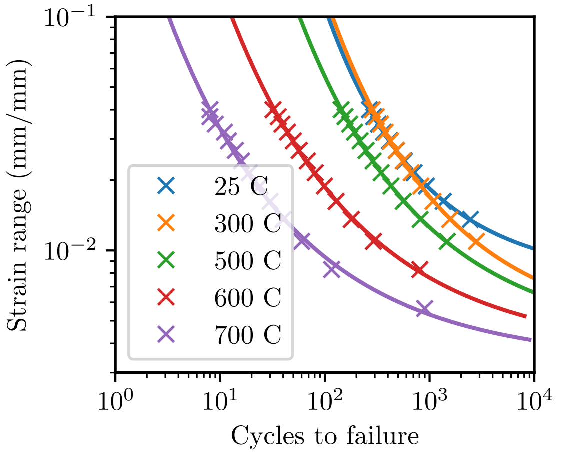

Figure 3.7: Design fatigue curves for the reference inelastic model at several different temperatures and a strain rate of $\dot{\varepsilon} = 10^{-3}\,\mathrm{s}^{-1}$. Curves are a best-fit polynomial through a series of simulated fatigue tests at different strain ranges.

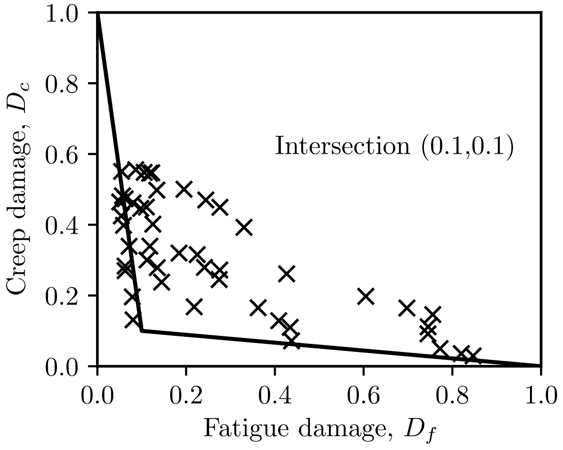

Figure 3.8: Design D-diagram for the reference material model. The diagram was constructed by plotting the results of a large series of creep-fatigue experiments, also shown on the figure.

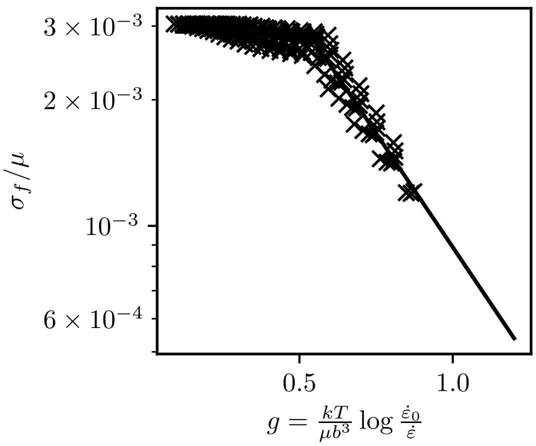

Figure 3.9: Kocks-Mecking diagram constructed by simulating uniaxial tension and creep tests with the reference inelastic model.

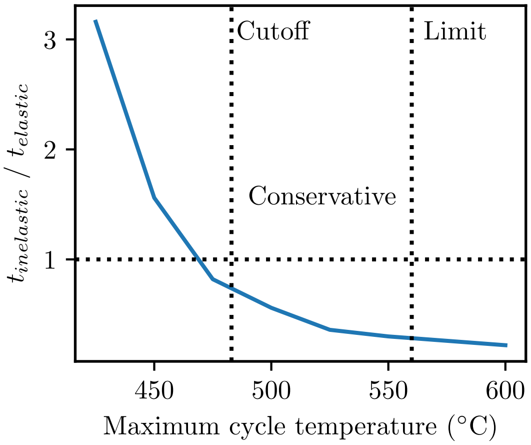

Figure 3.10: Diagram plotting the ratio between the Appendix HBB-T design life and the time to 1% strain computed by the inelastic model as a function of high cycle temperature.

4 Modifications to implement limits in the ASME Code

4.1 Supporting information

Chapter 2 describes a method for establishing the temperature at which, for a given strain rate, plastic deformation in a material becomes rate dependent. As argued in the introduction and in Chapter 3 this temperature should be established as an upper temperature limit for the use of the Section III, Division 5 design by elastic analysis provisions for the deformation controlled design limits addressing ratcheting strain accumulation and creep-fatigue damage.

While experimental data justifies the proposed approach there are several additional sources of corroborating information that could be used to support ASME Code action to implement the proposed design limits.

- The proposed temperature limits for 316H and 304H are very similar. This makes sense as these materials are both austenitic stainless steels with very similar material properties.
- The temperature limits for Grade 91 steel is relatively low, implying this material behaves viscoplastically at relatively low temperatures. This material behavior is well-known and currently alluded to in Division 5, for example in HBB-3214.2.
- The proposed upper temperature limit for Alloy 617 for 645° C is very close to an existing restriction on the use of design by elastic analysis above 650° for this material in the proposed Section III, Division 5 Code Case allowing the use of this material in elevated temperature design.
- When used to predict the material yield stress as a function of temperature and at the ASTM E-21 strain rate the Kocks-Mecking models for the Class A materials agree with the average material yield stress as characterized by the data underlying the ASME values of S_y. Figure 4.1 shows this comparison for Grade 91. Likely some of the data points are duplicated in the Kocks-Mecking plot and the yield stress data, however many of the data points are independent.
- The temperature limits derived and proposed here agree substantially with limits derived previously through a more approximate method. This previous work is described in detail in Appendix A. With the exception of Grade 91, these previous temperature limits match the current proposal to within 25° F. For more details and some comments on why the Grade 91 limits may diverge refer to the appendix.

4.2 Potential Code changes

Table 4.1 summarizes the proposed upper temperature limits to be applied to the design by elastic analysis provision in Nonmandatory Appendix HBB-T. The table presents the cutoffs in both standard and metric units in the format used in Section III of the Code.

Implementing these temperature limits would require Code action to change the language of HBB-T as well as the proposed Alloy 617 Code Case. Table 4.1 would be inserted into HBB-T as Table HBB-T-1321. Provision HBB-T-1321 would be amended to read "The

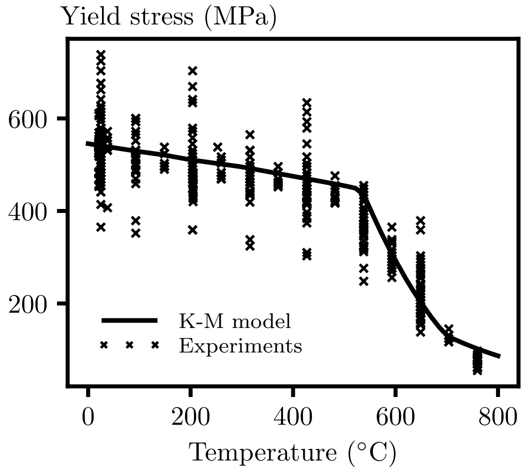

Figure 4.1: Comparison between the data underlying the ASME Code values of yield stress (S_y) for the Grade 91 and the Kocks-Mecking model predictions for flow stress at the ASTM E-21 strain rate of $8.33 \times 10^{-5}\,\mathrm{s}^{-1}$.

Material	Maximum Temperature, °F (°C)
304 SS	1160 (625)
316 SS	1185 (640)
Ni-Fe-Cr (Alloy 800H)	1310 (710)
2¼Cr-1Mo	1025 (550)
9Cr-1Mo-V	845 (450)
Alloy 617	1195 (645)

Table 4.1: Recommended Code temperature cutoff table.

strain limits of HBB-T-1310 are considered to have been satisfied if the limits of any one of HBB-T-1322, HBB-T-1323, or HBB-T-1324 are satisfied *and the maximum cycle temperature does not exceed the limits in Table HBB-T-1321*." The modified Code language is given here in italics.

The first paragraph of HBB-T-1311 would be amended to read "The strain limits of HBB-T-1310 are considered to have been satisfied if the limits of HBB-T-1332 are satisfied in addition to (a) through (h) below *and the maximum cycle temperature does not exceed the limits in Table HBB-T-1321*."

Finally, provision HBB-T-1431 would be amended to add the following item to the existing list of restrictions: "*(4) The maximum cycle temperature does not exceed the limits in Table HBB-T-1321*."

Corresponding changes could be made to the Alloy 617 Code Case.

5 Conclusions

5.1 Effects of implementing the temperature limits

The proposed temperature limits describe when plastic deformation in the materials becomes rate sensitive. They do not directly relate to the performance of the materials under elevated temperature service conditions. Rather, they describe when, at some fixed, representative deformation rate thermal mechanisms become significant in the processes of microstructural dislocation motion. The temperature then will depend strongly on the initial material microstructure. For example, Grade 91 has a meta-stable initial microstructure consisting of a hierarchical arrangement of martensite laths arranged inside large prior austenite grains [15, 25]. Unsurprisingly, the high obstacle density and meta-stable nature of this initial structure means thermal activation energy plays a strong role in dislocation motion in Grade 91 even at relatively low temperatures. The proposed temperature limit for Grade 91 reflects this fact as it is relatively low compared to the material's Division 5 maximum use temperature.

The effect of implementing the proposed temperature limits is then also material dependent. For 2.25Cr-1Mo the proposed temperature limit does not affect the existing HBB design process at all as the proposed cutoff temperature is higher than the Division 5 maximum use temperature. For Grade 91 the temperature limit would significantly affect design as it is below the likely use temperature for the material in many high temperature reactor designs.

The effect on the remaining Class A materials and Alloy 617 falls somewhere between these two extremes. The proposed cutoff temperatures are below the material maximum use temperature but likely above the expected operating temperatures for these materials in some reactor designs.

Implementing temperature restrictions on the use of the Nonmandatory Appendix HBB-T design by elastic analysis methods does not cripple the Code design procedures. The designer can always fall back on the design by inelastic analysis provisions to meet the Code deformation controlled quantity design limits. Additionally, Code Cases N-861 and N-862 provide simplified design methods based on elastic perfectly plastic (EPP) analysis for 304H and 316H [4, 5]. The EPP methods are included in the proposed Alloy 617 Code Case and current work is extending these approaches to the remaining HBB Class A materials. The bounding theories underlying these methods do not directly rely on a decoupled model of creep-plasticity and so these methods may be reliable above the proposed cutoffs [11–14]. However, further work is needed to demonstrate their effectiveness at very high temperatures.

5.2 Summary

This report proposes upper temperature limits for the design by elastic analysis methods in Section III, Division 5, Nonmandatory Appendix HBB-T. The temperature limits are the point at which plastic deformation in each material becomes rate sensitive at a representative strain rate of $10^{-7}\,\mathrm{s}^{-1}$. As demonstrated in Chapters 1 and 3 such a limit may be required on the elastic analysis methods because they are based on bounding theories that assume a non-unified, decoupled model of creep-plasticity. If plastic deformation is rate sensitive then creep and plasticity are coupled deformation modes and the theories may not conservatively bound deformation and creep-fatigue damage, leading to potentially non-conservative designs.

Chapter 3 examines the theory underlying the Appendix T design by elastic analysis rules and identifies provisions where a unified creep-plasticity response would undermine the technical basis of the Code rules. Additionally, that chapter provides an explicit example of nonconservatism in the existing Code design rules above the proposed upper temperature limits with a comparison to full inelastic analysis.

Finally, Chapter 4 describes the Code changes that would be required to implement the proposed temperature cutoffs and summarizes a variety of collaborating evidence for the proposed cutoffs.

This report provides the technical basis required to propose the implementing Code changes to the relevant ASME BP&V Code Committees. There is one remaining issue that requires further study before implementing the proposed limits. The HBB-T methods include additional conservatism beyond the underlying bounding methods to account for material property variation and structural and loading uncertainties. To our knowledge there have been no studies to directly assess the margin of the HBB-T rules to determine how much of this added conservatism is required to bound quantifiable design uncertainties and how much effectively is extra margin or over conservatism. It seems likely the HBB-T rules are in fact over conservative. In that case some of this extra margin could be retained and used to increase the rigorous temperature limits established here.

Acknowledgments

The research was sponsored by the U.S. Department of Energy (DOE), under Contract No. DE-AC02-06CH11357 with Argonne National Laboratory, managed and operated by UChicago Argonne LLC. Programmatic direction was provided by the Office of Advanced Reactor Technologies (ART) of the Office of Nuclear Energy (NE).

The authors thank Robert Jetter for providing the appendix describing previous work on establishing temperature limits.

Bibliography

[1] Vivek Agarwal, Richard N Wright, and Timothy Roney. Prediction of the Creep-Fatigue Lifetime of Alloy 617 : an Application of Non-Destructive Evaluation and Information Integration. In *Proceedings of the 22nd Conference on Structural Mechanics in Reactor Technology*, 2013.

[2] C. Albertini, M. Montagnani, E. V. Pizzinato, and A. Rodis. Comparison of the equivalent flow curves in tension and shear at low and high strain rate for AISI 316 and ARMCO iron. In *Transactions of the 11th international conference on structural mechanics in reactor technology*, pages 103–108, 1991.

[3] American Society of Mechanical Engineers. Section II, Part D (Metric). In *ASME Boiler and Pressure Vessel Code*. 2015.

[4] American Society of Mechanical Engineers. Case N-861: Satisfaction of Strain Limits for Division 5 Class A Components at Elevated Temperature Service Using Elastic-Perfectly Plastic Analysis. In *ASME Boiler and Pressure Vessel Code, Nuclear Component Code Cases*. 2015.

[5] American Society of Mechanical Engineers. Case N-862: Calculation of Creep-Fatigue for Division 5 Class A Components at Elevated Temperature Service Using Elastic-Perfectly Plastic Analysis. In *ASME Boiler and Pressure Vessel Code, Nuclear Component Code Cases*. 2015.

[6] American Society of Mechanical Engineers. Section III, Division 5. In *ASME Boiler and Pressure Vessel Code*. 2017.

[7] Tai Asayama and Yukio Tachibana. Existing Evaluation Procedures for Grade 91 and Hastelloy XR. Technical report, ASME STP-NU-018, 2009.

[8] ASTM International. E 21-09: Standard Test Methods for Elevated Temperature Tension Tests of Metallic Materials, 2009.

[9] J Bree. Elastic-plastic behaviour of thin tubes subjected to internal pressure and intermittent high-heat fluxes with application to fast-nuclear-reactor fuel elements. *The Journal of Strain Analysis for Engineering Design*, 2(3):226–238, 1967.

[10] J Bree. Incremental Growth Due To Creep And Plastic Yielding Of Thin Tubes Subjected To Internal Pressure And Cyclic Thermal Stresses. *Journal of Strain Analysis for Engineering Design*, 3(2):122–127, 1968.

[11] Peter Carter. Analysis of cyclic creep and rupture. Part 1: Bounding theorems and cyclic reference stresses. *International Journal of Pressure Vessels and Piping*, 82(1): 15–26, 2005.

[12] Peter Carter. Analysis of cyclic creep and rupture. Part 2: Calculation of cyclic reference stresses and ratcheting interaction diagrams. *International Journal of Pressure Vessels and Piping*, 82(1):27–33, 2005.

[13] Peter Carter, R. I. Jetter, and T.-L. Sham. Application of shakedown analysis to evaluation of creep-fatigue limits. In *Proceedings of the ASME 2012*, pages 1–10, 2012.

[14] Peter Carter, R. I. Jetter, and T.-L. Sham. Verification of elastic-perfectly plastic methods for evaluation of strain limits - analytical comparisons. In *Proceedings of the ASME 2014 Pressure Vessels & Piping Conference*, pages 1–8, 2014.

[15] E Cerri, E Evangelista, S Spigarelli, and P Bianchi. Evolution of microstructure in a modified 9Cr-1Mo steel during short term creep. *Materials Science and Engineering: A*, 245(2):285–292, 1998.

[16] J. L. Chaboche. A review of some plasticity and viscoplasticity constitutive theories. *International Journal of Plasticity*, 24(10):1642–1693, oct 2008.

[17] J.L. Chaboche. Constitutive equations for cyclic plasticty and cyclic viscoplasticity. *International Journal of Plasticity*, 5:247–302, 1989.

[18] S. A. Chavez, G. E. Korth, D. M. Harper, and T. J. Walker. High-temperature tensile and creep data for Inconel 600, 304 stainless steel and SA106B carbon steel. *Nuclear Engineering and Design*, 148:351–363, 1994.

[19] I. W. Chen and A. S. Argon. Creep cavitation in 304 stainless steel. *Acta Metallurgica*, 29(7):1321–1333, 1981.

[20] B. K. Choudhary and E. Isaac Samuel. Creep behaviour of modified 9Cr-1Mo ferritic steel. *Journal of Nuclear Materials*, 412(1):82–89, 2011.

[21] T. S. DeSisto and F. L. Carr. Low temperature mechanical properties of 300 series stainless steels and titanium. Technical report, Watertown Arsenal Laboratories, 1961.

[22] D. C. Drucker. A definition of a stable inelastic material. *ASME Journal of Applied Mechanics*, 6:236–249, 1959.

[23] A. Fookes, S. X. Li, D. J. Smith, and M. W. Spindler. Stress Relaxation during Dwells for Creep and Fatigue Cycling of Type 316H Stainless Steel at 550C. In *2nd International ECCC Conference*, 2009.

[24] C. O. Frederick and P. J. Armstrong. Convergent internal stresses and steady cyclic states of stress. *The Journal of Strain Analysis for Engineering Design*, 1(2):154–159, 1966.

[25] B. G. Gieseke, C. R. Brinkman, and P. J. Maziasz. The influence of thermal aging on the microstructure and fatigue properties of modified 9Cr-1Mo steel. In *TMS The Minerals, Metals & Materials Society*, 1993.

[26] J. P. Hammond and V. K. Sikka. Heat-to-heat variations of total strain (to 5%) at discrete stress levels in types 316 and 304 stainless steel from 24 to 316 C. Technical report, Oak Ridge National Laboratory, 1976.

[27] JA Horak, VK Sikka, and DT Raske. Review of mechanical properties and microstructures of Types 304 and 316 stainless steel after long-term aging. Technical report, Oak Ridge National Laboratory, 1983.

[28] R. Hormozi, F. Biglari, and K. Nikbin. Experimental and numerical creep-fatigue study of Type 316 stainless steel failure under high temperature LCF loading condition with different hold time. *Engineering Fracture Mechanics*, 141:19–43, 2015.

[29] L. M. Kachanov. On the creep fracture time. *Izv Akad, Nauk USSR Otd Tech*, 8:23–31, 1958.

[30] K. Kanazawa and S. Yoshida. Creep and Fatigue in Elevated Temperature Applications. *Institution of Mechanical Engineers*, 1:C226, 1974.

[31] Jong Bum Kim, Hyeong Yeon Lee, Chang Gyu Park, and Jae Han Lee. Creep-fatigue test of a SA 316SS structure and comparative damage evaluations based upon elastic and inelastic approaches. *International Journal of Pressure Vessels and Piping*, 85(8): 550–556, 2008.

[32] S Kim and J R Weertman. Investigation of Microstructural Changes in a Ferritic Steel Caused by High Temperature Fatigue. *Metallurgical Transactions*, 19A(April):999–1007, 1988.

[33] K. Kimura, H. Kushima, and K. Sawada. Long-term creep deformation property of modified 9Cr-1Mo steel. *Materials Science and Engineering A*, 510-511(C):58–63, 2009.

[34] R. L. Klueh. Heat-to-heat variation of tensile properties of annealed 2 1/4 Cr-1 Mo steel. Technical report, Oak Ridge National Laboratory ORNL/TM-5906, 1977.

[35] R. L. Klueh and R. E. Oakes. High-strain-rate tensile properties of annealed 2 1/4 Cr-1 Mo steel. Technical report, Oak Ridge National Laboratory ORNL-TM-5028, 1975.

[36] U F Kocks. Realistic constitutive relation for metal plasticity. *Materials Science and Engineering A*, 317:181–187, 2001.

[37] U. F. Kocks, A. S. Argon, and M. F. Ashby. Thermodynamics and kinetics of slip. In B. Chalmers, J. W. Christian, and T. B. Massalski, editors, *Progress in Materials Science*, pages 64–291. 1975.

[38] Gyeong H. Koo and Ji Hyun Kwon. Identification of inelastic material parameters for modified 9Cr-1Mo steel applicable to the plastic and viscoplastic constitutive equations. *International Journal of Pressure Vessels and Piping*, 88(1):26–33, 2011.

[39] E. Krempl. An Experimental Study of Room-Temperature Creep and Relaxation of AISI Type 304 Stainless. *Journal of the Mechanics and Physics of Solids*, 27:363–375, 1979.

[40] S. Latha, M. Nandagopal, S. Panneer Selvi, K. Laha, and M. D. Mathew. Tensile and creep behaviour of modified 9Cr-1Mo steel cladding tube for fast reactor using metallic fuel. *Procedia Engineering*, 86:71–79, 2014.

[41] F. A. Leckie and D. R. Hayhurst. Creep rupture of structures. *Proceedings of the Royal Society A: Mathematical, Physical and Engineering Sciences*, 340:323–347, 1974.

[42] Kouichi Maruyama, Junya Nakamura, Kyosuke Yoshimi, and Yuji Nagae. Evaluation of long-term creep rupture life of Gr.91 steel by analysis of on-going creep curves. In *Proceedings from the Eighth International Conference on Advances in Materials Technoglogy for Fossil Power Plants*, pages 467–478, 2016.

[43] H Mecking, B Nicklas, N. Zarubova, and U F Kocks. A "universal" temperature scale for plastic flow. *Acta Metallurgica*, 34(3):527–535, 1986.

[44] M. C. Messner, V.-T. Phan, and T.-L. Sham. FY17 Status Report on the Initial Development of a Constitutive Model for Grade 91 Steel. Technical Report ANL-ART-93, Argonne National Laboratory, 2017.

[45] M Mizuno. Uniaxial ratchetting of 316FR steel at room temperature – Part I: experiments. *Journal of Engineering Materials and Technology*, 122(January 2000):29–34, 2000.

[46] Subhasish Mohanty, William K. Soppet, Saurindranath Majumdar, and Krishnamurti Natesan. In-air and pressurized water reactor environment fatigue experiments of 316 stainless steel to study the effect of environment on cyclic hardening. *Journal of Nuclear Materials*, 473:290–299, 2016.

[47] W. J. O'Donnell and J. S. Porowski. Upper Bounds for Accumulated Strains Due to Creep Ratcheting. *Journal of Pressure Vessel Technology*, 96(3):150–154, 1974.

[48] Toshio Ohba, Osamu Kanemaru, Koichi Yagi, and Chiaki Tanaka. Long-term stress relaxation properties of NCF 800H Alloy. *Journal of the Society of Materials Science, Japan*, 46(1):19–24, 1997.

[49] N Ohno, M Abdel-Karim, M Kobayashi, and T Igari. Ratchetting characteristics of 316FR steel at high temperature, part I: Strain-controlled ratchetting experiments and simulations. *International Journal of Plasticity*, 14(4-5):355–372, 1998.

[50] Walter Osthoff, Hans Schuster, Philip J. Ennis, and Hubertus Nickel. Creep and relaxation behavior of Inconel-617. *Nuclear Technology*, 66(2), 1984.

[51] V. K. Sikka, B. L. P. Booker, M. K. Booker, and J. W. McEnerney. Tensile and Creep Data on Type 316 Stainless Steel. Technical report, Oak Ridge National Laboratory, 1980.

[52] R. W. Swindeman. Cyclic Stress-Strain-Time Response of a 9CMMo-V-Nb Pressure Vessel Steel at High Temperature. In H. D. Solomon, G. R. Halford, L. R. Kaisand, and B. N. Leis, editors, *Low Cycle Fatigue, ASTM STP 942*, pages 107–122. American Society for Testing and Materials, Philadelphia, 1988.

[53] R. W. Swindeman. Construction of isochronous stress-strain curves for 9Cr-1Mo-V Steel. *Advances in Life Prediction Methodology*, 391:95–100, 1999.

[54] R. W. Swindeman and R. L. Klueh. Relaxation behavior of 2 1/4 Cr-1 Mo steel under multiple loading. Technical report, Oak Ridge National Laboratory ORNL/TM-6048, 1977.

[55] R. W. Swindeman and R. L. Klueh. Constant- and variable-stress creep tests on 2-1/4 Cr-1 Mo steel at 538 C. *Res Mechanica*, 3:245–270, 1981.

[56] Yukio Takahashi, Hiroshi Shibamoto, and Kazuhiko Inoue. Long-term creep rupture behavior of smoothed and notched bar specimens of low-carbon nitrogen-controlled 316 stainless steel (316FR) and their evaluation. *Nuclear Engineering and Design*, 238(2): 310–321, 2008.

[57] S. Timoshenko and S. Woinowsky-Krieger. *The Theory of Plates and Shells*. McGraw Hill, New York, 2nd edition, 1959.

[58] Y. Q. Wang, M. W. Spindler, C. E. Truman, and D. J. Smith. Critical analysis of the prediction of stress relaxation from forward creep of Type 316H austenitic stainless steel. *Materials and Design*, 95:656–668, 2016.

[59] D. S. Wood and K. Williamson. Deformation behaviour of type 316 steel at 400 C. Technical report, Risley Nuclear Power Development Establishment, 1982.

[60] D. S. Wood, A. B. Baldwin, T. J. Sarbutts, and K. Williamson. The low temperature deformation behavior of type 316 steel. In *Materials for nuclear reactor core applications*, pages 2–7. 1987.

[61] M. Yaguchi and Y. Takahashi. Unified Inelastic Constitutive Model for Modified 9Cr-1Mo Steel Incorporating Dynamic Strain Aging Effect. *JSME International Journal, Series A*, 42(1):1–10, 1999.

[62] Masatsugu Yaguchi and Yukio Takahashi. Ratchetting of viscoplastic material with cyclic softening, part 1: Experiments on modified 9Cr-1Mo steel. *International Journal of Plasticity*, 21(1):43–65, 2005.

[63] M. Yamashita and Y. Wada. The Stress-Relaxation Behavior of Type 304 Stainless. *International Journal of Pressure Vessels and Piping*, 42:203–216, 1990.

[64] Ji Hyun Yoon, Young Chun Kim, Seokmin Hong, Gyeong Hoi Koo, and Bong Sang Lee. Inelastic cyclic defonnation behaviors of type 316H stainless steel for reactor pressure vessel of sodium-cooled fast reactor at elevated temperatures. *Journal of Korean Institute of Metals and Materials*, 53(10):681–687, 2015.

[65] A. G. Youtsos, J. Donea, and G. Verzeletti. Viscoplastic behavior of stainless steels AISI 316L and 316H. *Acta Mechanica*, 76:161–187, 1989.

[66] Kuo Zhang and Jarir Aktaa. Characterization and modeling of the ratcheting behavior of the ferritic-martensitic steel P91. *Journal of Nuclear Materials*, 472:227–239, 2016.

[67] J. H. Zhu, D. Boerman, and G. Piatti. Strength of the AISI 316 Stainless Steel Above 800 C. In *Transactions of the 7th International Conference on Structural Mechanics in Reactor Technology*, pages 507–514, 1983.

A An alternative method for determining approximate temperature limits on the HBB-T simplified methods

The limitation on applicability of the simplified methods was first proposed in the original code case for Alloy 617 for elevated temperature Class 1 (now Class A) construction. The rationale for the restrictions was the lack of differentiation between plasticity and creep, that is the basis for the development of the current simplified rules for strain limit and creep-fatigue damage evaluation. One way of looking at this is that as the operating temperature increases, the value of yield strength used in the current simplified methods is no longer independent of strain rate. In the initial Alloy 617 Code Case, circa the 1990s, this value was deemed to be 1200° F for Alloy 617. Generally, it has been recognized that similar restrictions on applicability of the current simplified methods to other materials would be appropriate at very high temperatures, but there was not previously a defined approach as how to establish this limitation. The following approach was undertaken several years ago as a potential solution prior to the more rigorous approach documented in the body of this report. It was presented to the Working Group – Creep-Fatigue and Negligible Creep (WG-CFNC) to illustrate the trend of the data and highlight potential problem areas.

For this brief study a nominal standard tensile strain rate of $1.0 \times 10^{-4}\,\mathrm{s}^{-1}$ was assumed. For a design strain of about 0.1 – 0.2% this would roughly correspond to a transient duration of 10 – 20 seconds which would be representative of a very rapid, off normal, i.e. Service Level B or C, event in a sodium system. A normal event, i.e. Service Level A, would be at least an order of magnitude slower.

Material	1 hr (° F)	10 hr (° F)	Recommended (° F)
304SS	1225	1225	1175
316SS	1250	1150	1200
800H	1325	1250	1300
2.25Cr-1Mo	1000	1000	1000
Grade 91	950 [1]	950	965

Table A.1: Transition temperatures for the Class A materials.

While it would be best to have direct test data, there isnt that much available for the Class A materials and range of potential operating conditions. Accordingly, it was assumed that an approximate representation could be obtained using the isochronous stress strain curves ISSCs) with an allowable yield strength reduction of 10%. To make use of the available plots with minimal interpolation, the 1 hr curves were taken as representative of off normal events and the 10 hr curves representative of normal events.

Based on the above, the procedure is to take the 0.2% offset yield strength from the hot tensile ISSC and project it vertically downward to the 1 hr and 10 hr ISSCs. If the intercept of the applicable ISSC is less than 10% below the 0.2% offset yield strength from the hot tensile ISSC, the process is repeated at the next higher temperature ISSC and vice-versa if it is greater than 10% lower. In some cases it is necessary to roughly interpolate between ISSCs.

---

[1] There is a significant change in the Grade 91 isochronous stress-strain curves going from 950° F to 1000° F. At 950° F there is not a big loss in strength between the hot tensile curve and the 1 hr ISSC; however, there is a big drop at 1000° F.

Table A.1 summarizes the resulting approximations. The recommended value is a rough, rounded average of the 1 hr and 10 hr intercepts based on the desire to have a single, representative temperature limit.

Distribution List

Name	*Affiliation*	*Email*
Caponiti, A.	DOE	alice.caponiti@nuclear.energy.gov
Croson, D.	INL	diane.croson@inl.gov
Gouger, H. D.	INL	hans.gougar@inl.gov
Hill, R. N.	ANL	bobhill@anl.gov
Krumdick, G. K.	ANL	gkrumdick@anl.gov
Lesica, S.	DOE	sue.lesica@nuclear.energy.gov
Li, D.	DOE	diana.li@nuclear.energy.gov
McMurtrey, M.	INL	michael.mcmurtrey@inl.gov
Messner, M. C.	ANL	messner@anl.gov
Qualls, A. L.	ORNL	quallsal@ornl.gov
Sham, T.-L.	ANL	ssham@anl.gov
Singh, D.	ANL	dsingh@anl.gov
Travis, T. R.	INL	travis.mitchell@inl.gov
Wang, Y.	ORNL	wangy2@ornl.gov
Wright, R.	INL	richard.wright@inl.gov
Zhang, X.	ANL	xuanzhang@anl.gov

Applied Materials Division
Argonne National Laboratory
9700 South Cass Avenue, Bldg. 208
Argonne, IL 60439

www.anl.gov

Argonne National Laboratory is a U.S. Department of Energy
laboratory managed by UChicago Argonne, LLC